Hyperspectral Tensor Completion Using Low-Rank Modeling and Convex Functional Analysis

Chia-Hsiang Lin, *Member, IEEE*, Yangrui Liu, *Student Member, IEEE*, Chong-Yung Chi, *Life Fellow, IEEE*, Chih-Chung Hsu, *Senior Member, IEEE*, Hsuan Ren, *Senior Member, IEEE*, and Tony Q. S. Quek, *Fellow, IEEE*

***Abstract*— Hyperspectral tensor completion (HTC) for remote sensing, critical for advancing space exploration and other satellite imaging technologies, has drawn considerable attention from recent machine learning community. Hyperspectral image (HSI) contains a wide range of narrowly spaced spectral bands hence forming unique electrical magnetic signatures for distinct materials, and thus plays an irreplaceable role in remote material identification. Nevertheless, remotely acquired HSIs are of low data purity and quite often incompletely observed or corrupted during transmission. Therefore, completing the 3-D hyperspectral tensor, involving two spatial dimensions and one spectral dimension, is a crucial signal processing task for facilitating the subsequent applications. Benchmark HTC methods rely on either supervised learning or nonconvex optimization. As reported in recent machine learning literature, John ellipsoid (JE) in functional analysis is a fundamental topology for effective hyperspectral analysis. We therefore attempt to adopt this key topology in this work, but this induces a dilemma that the computation of JE requires the complete information of the entire HSI tensor that is, however, unavailable under the HTC problem setting. We resolve the dilemma, decouple HTC into convex subproblems ensuring computational efficiency, and show state-of-the-art HTC performances of our algorithm. We also demonstrate that our method has improved the subsequent land cover classification accuracy on the recovered hyperspectral tensor.**

***Index Terms*— Convex optimization, functional analysis, hyperspectral image (HSI), John ellipsoid (JE), tensor completion.**

Manuscript received 22 March 2022; revised 3 September 2022 and 23 December 2022; accepted 6 February 2023. This work was supported in part by the Young Scholar Fellowship Program (Einstein Program) of Ministry of Science and Technology (MOST) in Taiwan under Grant MOST 111-2636-E-006-028, in part by the Higher Education Sprout Project of Ministry of Education (MOE) to the Headquarters of University Advancement at National Cheng Kung University (NCKU), and in part by the Center for Data Science (CDS) at NCKU. *(Corresponding author: Chia-Hsiang Lin.)*

Chia-Hsiang Lin and Yangrui Liu are with the Department of Electrical Engineering, National Cheng Kung University, Tainan 70101, Taiwan (e-mail: chiahsiang.steven.lin@gmail.com; q38103501@gs.ncku.edu.tw).

Chong-Yung Chi is with the Department of Electrical Engineering, National Tsing Hua University, Hsinchu 300044, Taiwan (e-mail: cychi@ee.nthu.edu.tw).

Chih-Chung Hsu is with the Department of Statistics, National Cheng Kung University, Tainan 70101, Taiwan (e-mail: cchsu@gs.ncku.edu.tw).

Hsuan Ren is with the Center for Space and Remote Sensing Research, National Central University, Taoyuan 320317, Taiwan (e-mail: hren@csrsr.ncu.edu.tw).

Tony Q. S. Quek is with the Information Systems Technology and Design Pillar, Singapore University of Technology and Design, Singapore 487372, and also with the Department of Computer Science and Information Engineering, National Cheng Kung University, Tainan 70101, Taiwan (e-mail: tonyquek@sutd.edu.sg).

Color versions of one or more figures in this article are available at https://doi.org/10.1109/TNNLS.2023.3243808.

Digital Object Identifier 10.1109/TNNLS.2023.3243808

I. Introduction

HYPERSPECTRAL tensor completion (HTC) has received considerable attention in recent machine learning community, mainly owing to its irreplaceable role in accurate computer vision and remote material identification, both are fundamentally important for advancing space exploration and other satellite imaging technologies [1], [2], [3], [4]. An elegant connection between the blind source separation (BSS), an unsupervised learning technique having early rooted in neural networks [5], and the HTC problem will also be seen later. Hyperspectral image (HSI) data cube, acquiring electrical magnetic information across a continuously distributed spectral range, can be mathematically formulated as a 3-D tensor containing two spatial dimensions and one spectral dimension. HSI has outstanding capability in material identification because the acquired wide spectrum information allows depicting unique spectral signatures for distinct materials [6], [7].

Various HSI analysis technologies have found numerous real-world applications, including urban planning, mineral mapping, military detection, precision agriculture, just to name a few. Nevertheless, remotely acquired HSIs are quite often incompletely observed due to broken satellite/airborne sensors, or may be damaged during the transmission from space to the ground stations, resulting in dead pixels and stripe-corrupted images. To facilitate subsequent HSI analysis, and considering the lack of high-quality big data due to expensive hyperspectral satellite/airborne image acquisitions, designing unsupervised HTC theory/method for blindly and effectively reconstructing the HSI data becomes an indispensable research line in this flourishing age of space development.

Obviously, the HTC problem amounts to an ill-posed inverse problem, and thus typical regularizers (e.g., the total variation (TV) function) are often applied to regularize this image restoration problem [8], [9]. On the other hand, the high spatial and spectral correlations of typical HSI data can also be used to mitigate such an ill-posedness by considering the HSI data as a low-rank matrix/tensor [10], [11], [12]. For example, the low-rank matrix factorization-based TV-regularized (LRTV) hyperspectral restoration method has used both the naive TV and the spatial/spectral correlations [13]. A related method proposed in [9] is based on local low-rankness and global TV to address the HTC problem. Another method of the low-rank-based single-image decomposition (LRSID) model [14] proposed to group nonoverlapping patches with spectral similarity for extracting the embedded low-rank structure. Hyperspectral unmixing technique, for separating mixed

hyperspectral signatures from their mixtures, also naturally arises to reveal such a low-rankness in the HTC algorithm design [15], [16]. For example, by selecting the pure pixels as endmembers of the HSI, the unmixing-based inpainting (UBI) method proposed in [17] recovers the corrupted HSI by linearly decomposing and reconstructing the data cube. However, pure pixels are often lacking in the remotely acquired HSI data, making the associated HTC methods ineffective.

Due to the huge volume of typical HSI data, numerous low-rank decomposition methods were proposed to reduce the computational complexity of the devised HTC algorithm by extracting main features such as principal component analysis (PCA) [18], [19]. To preserve the spatial structure of the recovered HSI, some works further adopt tensor decomposition technologies for the feature extraction task [20], [21], [22], [23]. In the Kronecker basis representation-based tensor completion (KBRTC) method [21], the sparsity insights delivered by both the Tucker and CANDECOMP/PARAFAC (CP) decompositions are blended to design a new sparsity measure considering different modes of low-rankness. Another method, termed as global–local image characterization with noise modeling, preprocesses the HSI by a fast denoising convolutional neural network and also exploits the sparsity prior with low-rankness at the tensor level in its inpainting criterion [24]. Another denoising-based HTC method is called fast hyperspectral image inpainting (FastHyIn) [25], which exploits the self-similarity (SS) nature to recover the corrupted HSI tensor, where SS refers to the property of natural images containing many nonlocal patches of similar color, texture, and geometric structure. However, as the image SS induces a nonconvex optimization problem that is not explicitly defined, such method does not have convergence guarantee in general [26]. Usually, implementing an implicitly defined criterion requires the so-called plug-and-play strategy in the machine learning literature; for example, FastHyIn plugs the block matching 3-D (BM3D) denoiser in solving an iterative algorithmic step [25], [27].

In this work, instead of considering those widely adopted nonconvex frameworks [28], [29], we aim to propose an unsupervised convex HTC algorithm without relying on big data or the existence of pure pixels, implying a more practical method for remote sensing applications. In hyperspectral analysis literature, the most well-known theory with robustness against the lack of pure pixels would be the one based on the Craig simplex (CS) criterion [15], [30]. However, the CS criterion is known to be nonconvex and induces an NP-hard problem. This motivates us to introduce the John ellipsoid (JE) criterion into the HTC algorithm design for the first time. JE is a key topology in functional analysis, and it is defined as the maximum-volume ellipsoid inscribed in the data convex hull (i.e., convex hull of the pixel vectors). The JE criterion can be transformed into a convex conic optimization problem, and it is theoretically and experimentally provable to be robust against the lack of pure pixels [31]. More specifically, following the definition of the data purity γ proposed in [32], the aforementioned pure pixel assumption is theoretically equivalent to "$\gamma = 1$," while JE has perfect endmember identifiability whenever the much milder condition "$\gamma > 1/\sqrt{N-1}$" holds true; here, N is the number of materials presented in the HSI [3], [32], [33].

These remarkable properties have distinguished the convex JE criterion, whose fundamental role in hyperspectral analysis is thus revealed in recent mathematics and machine learning literature [3], [34]. Though JE possesses the above-mentioned fundamental advantages, implementing the JE criterion requires the full information of the HSI, leading to a dilemma in the HTC problem wherein the pixels are not completely observed. For the first time, we successfully adopt the JE theory to solve the challenging HTC problem, and the superiority of the proposed algorithm will be demonstrated using extensive experimental evidences. Furthermore, besides showing the state-of-the-art HTC performances, we also show that our method has improved the subsequent classification accuracy on the recovered hyperspectral tensor.

The remaining parts of this article are organized as follows. In Section II, we design the JE-based HTC algorithm under convex optimization framework. Extensive experimental results are presented and discussed in Section III, where we also show that performing the classification on the HSI reconstructed by our HTC method does yield better accuracy. Finally, conclusions are drawn in Section IV.

For better readability, some standard notations used in this article are collectively summarized hereinafter. For any given positive integer Z, $\mathcal{I}_Z$ is defined as $\mathcal{I}_Z \triangleq \{1, \ldots, Z\}$. $\text{conv}(\mathcal{S})$ denotes the convex hull of the set $\mathcal{S}$ [31]. $\mathbb{R}^N$ is the N-dimensional Euclidean space, $\mathbb{R}^{M\times N}$ is the $(M \times N)$-dimensional real-valued matrix space, and $\mathbb{R}^{M\times N\times L}$ is the $(M \times N \times L)$-dimensional real-valued three-way tensor space. $\boldsymbol{e}_i^{(N)}$ is the ith unit vector of $\mathbb{R}^N$. $\mathbf{1}$ is the all-one vector/matrix/tensor with dimensionality specified in its subscript. $[\mathbf{X}]_{l_1,l_2,\ldots,l_N}$ is the $(l_i, l_2, \ldots, l_N)$th entry of the N-way tensor $\mathbf{X}$. $\boldsymbol{M}^{\mathrm{T}}$ is the transpose of the matrix $\boldsymbol{M}$, and $\boldsymbol{M}^{-1}$ is the inverse of the matrix $\boldsymbol{M}$. $\sup \mathcal{S}$ denotes the supremum of a given set $\mathcal{S}$ [31]. $\|\cdot\|_2$ and $\|\cdot\|_F$ denote the ℓ_2-norm and Frobenius norm, respectively.

II. JE-Based Hyperspectral Tensor Completion

A. Problem Definition and Reformulation

HSI can be considered as a three-way tensor, with two spatial dimensions and one spectral dimension, as illustrated in Fig. 1. Specifically, an HSI tensor $\mathbf{X} \in \mathbb{R}^{L_1\times L_2\times M}$ contains $L = L_1L_2$ pixels across M spectral bands. In hyperspectral remote sensing, the HSI tensor is often incompletely acquired. For convenience, define the support

$$\boldsymbol{\Omega} \subseteq \{(\ell_1, \ell_2, m) | \ell_1 \in \mathcal{I}_{L_1}, \ell_2 \in \mathcal{I}_{L_2}, m \in \mathcal{I}_M\}$$

as the set of indices of those observable entries in $\mathbf{X}$. Also, define its complement set $\overline{\boldsymbol{\Omega}} \triangleq \{(\ell_1, \ell_2, m) | \ell_1 \in \mathcal{I}_{L_1}, \ell_2 \in \mathcal{I}_{L_2}, m \in \mathcal{I}_M\} \setminus \boldsymbol{\Omega}$ corresponding to missing data, where "$\setminus$" denotes the set difference operator. In practice, determining $\boldsymbol{\Omega}$ may be nontrivial especially when the corrupted pixels are densely populated [cf., the left region of Fig. 3(a)]. Theoretically, however, the only requirement of $\boldsymbol{\Omega}$ is to ensure that its complement (i.e., the mask $\overline{\boldsymbol{\Omega}}$) contains all the damaged entries. Although this simple requirement may result in a larger mask [cf., Fig. 3(b)], meaning a more difficult HTC task, the proposed method is empirically found to be robust against such situation; this can be seen from the large percentage of missing entries illustrated in Fig. 1. On the other hand, comparing to other methods that require exact mask information, the above

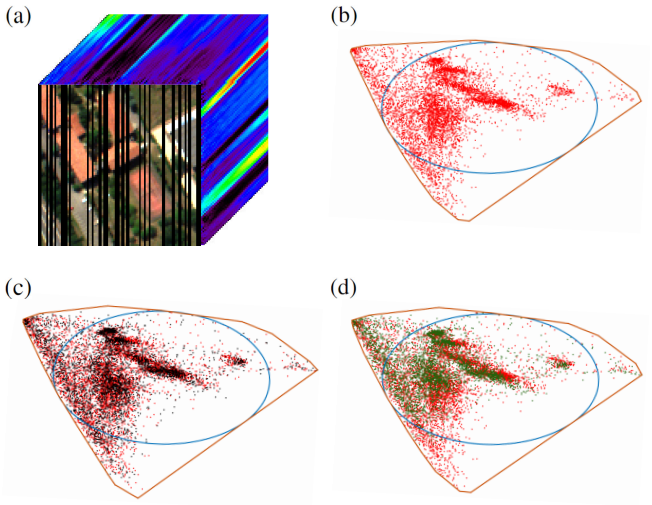

Fig. 1. Seriously corrupted HSI tensor is illustrated in (a), where HSI can be viewed as a three-way tensor; the first two spatial dimensions define the location of a pixel, while the third dimension is for spectral indexing. The pixel vectors in (a) are presented using 2-D visualization in (b), where the red dots are data pixels, the data convex hull is marked by the brown polytope, and the blue ellipsoid is the JE (i.e., the maximum-volume elliposid inscribed in the data convex hull). Those stripe-corrupted pixels $[\mathbf{X}]_{\ell_1,\ell_2,:}$ (i.e., pixels in $\overline{\mathbf{\Omega}}$) are further highlighted in (c) using black dots and are roughly inpainted as $[\widetilde{\mathbf{X}}]_{\ell_1,\ell_2,:}$ [cf., (4)] marked using the green dots in (d). As one can see from (c) and (d), the data distribution of $\mathbf{X}$ and $\widetilde{\mathbf{X}}$ is similar, implying the important empirical observation that their corresponding data convex hulls (and hence JEs) remain almost the same, even if there are up to 40% corrupted pixels in the HSI (a).

requirement is easily achievable in practice and thus user-friendly.

To understand our problem formulation, we need to further introduce the data purity γ mentioned in Section I. The data purity γ was originally defined in the hyperspectral remote sensing literature [32] (cf., Lemma 1 for the exact definition), having the following physical meaning.

1) The range of γ is within the interval $1/\sqrt{N} \le \gamma \le 1$, where N is the number of materials presented in the considered HSI. A higher value of γ indicates a higher data purity.
2) The upper bound $\gamma = 1$ corresponds to the purest case, known as the pure-pixel condition (PPC), which is seldom true in hyperspectral remote sensing due to the low image resolution caused by the far distance between the sensors and target objects.
3) The lower bound $\gamma = 1/\sqrt{N}$ corresponds to the case that the percentages of the N materials in a hyperspectral pixel are all $1/N$, namely, the most heavily mixed/impurest case.

As discussed in item 2) above, the PPC "$\gamma = 1$" is not a realistic assumption, motivating us to adopt CS or JE criteria, both work well with identifiability guarantee under the much milder condition "$\gamma > 1/\sqrt{N-1}$" [3], [32], [33]. Further considering that the CS criterion is nonconvex and NP-hard, this work will be developed under the JE framework that amounts to a convex optimization criterion [3]. Therefore, we can explicitly define our HTC problem as the recovery of $\mathbf{X}$ from the observable data $\mathbf{X}_{\mathbf{\Omega}} \triangleq \{[\mathbf{X}]_{\ell_1,\ell_2,m} | (\ell_1,\ell_2,m) \in \mathbf{\Omega}\}$, under the more realistic purity condition without involving nonconvex NP-hard optimizations. Below, we reformulate the HTC problem into the latent factor (LF) recovery problem, allowing us to adopt the powerful convex functional analysis to achieve the challenging HTC task.

Based on the well-known linear mixing model (LMM) [15], the (ℓ_1,ℓ_2)th pixel $[\mathbf{X}]_{\ell_1,\ell_2,:}$ can be modeled as a linear combination of hyperspectral signature vectors (a.k.a. endmembers) of the underlying materials in $\mathbf{X}$, i.e.,

$$[\mathbf{X}]_{\ell_1,\ell_2,:} = \sum_{n=1}^{N} [\mathbf{S}]_{\ell_1,\ell_2,n} \boldsymbol{a}_n \quad \forall (\ell_1,\ell_2) \in \mathcal{I}_{L_1} \times \mathcal{I}_{L_2}$$

where the three-way tensor $\mathbf{S} \in \mathbb{R}^{L_1 \times L_2 \times N}$ is called the material abundance tensor, N is the number of materials presented in the HSI (assumed known a priori [35], [36]), and $\boldsymbol{a}_n \in \mathbb{R}^M$ denotes the endmember signature of the nth material. Defining the endmember matrix $\boldsymbol{A} \triangleq [\boldsymbol{a}_1, \ldots, \boldsymbol{a}_N]$, the LMM can be concisely rewritten as follows:

$$\mathbf{X} = \mathbf{S} \times_3 \boldsymbol{A} \tag{1}$$

where $\times_3$ is known as the mode-3 multiplication; to be precise, the mode-n multiplication of a tensor $\mathbf{T}$ with a matrix $\boldsymbol{M}$ is to left-multiply $\boldsymbol{M}$ to each vector along dimension-n in $\mathbf{T}$, i.e., $[\mathbf{T} \times_n \boldsymbol{M}]_{i_1,\ldots,i_{n-1},j,i_{n+1},\ldots,i_N} \triangleq \sum_m \boldsymbol{M}_{j,m} [\mathbf{T}]_{i_1,\ldots,i_{n-1},m,i_{n+1},\ldots,i_N}$. Therefore, by (1), the recovery of $\mathbf{X}$ (from the observable data $\mathbf{X}_{\mathbf{\Omega}}$) can be pin down to the recovery of the endmember matrix $\boldsymbol{A}$ (detailed in Section II-C) and the recovery of the abundance tensor $\mathbf{S}$ (detailed in Section II-D).

B. Contributions, Related Works, and Historical Milestones in Estimating Hyperspectral Endmembers

As will be detailed in Sections II-C and II-D, both LFs $\boldsymbol{A}$ and $\mathbf{S}$ will be elegantly computed via convex optimization. The powerful effectiveness of convex optimization can be seen in very recent tensor completion literature [37], though the method therein is not applicable to solve the HTC problem. In fact, the method proposed in [37] is completely different from our HTC method, because the adopted integer-valued Poisson distribution [37] is violated by the real-valued nature of the reflectance values in the hyperspectral tensor. As a key contribution, our work avoids those probability priors of the data distribution; instead, we pursue a geometry-oriented algorithm by well using the nature of HSI.

To reflect another contribution and difference of our work, we need to mention some related low-rank tensor completion works (though not customized for hyperspectral tensor), including the methods based on CANDECOMP/PARAFAC (CP) rank [38], Tucker rank [39], [40], Tubal rank [41], [42], [43], tensor train rank [44], [45], tensor ring rank [46], and so on. Nevertheless, none of these decomposition models is customized based on the nature of hyperspectral tensor [47], [48]. Using the tensor singular value decomposition (t-SVD)-based method [41] for example, it induces three LF that are hard to be physically explained in terms of the hyperspectral nature, preventing us from elegantly solving the HTC problem. Another important issue is that models with fewer LFs are always desired in machine learning. Comparing to those models with more than three LFs, our HTC theory involves only two physically explainable LFs $(\boldsymbol{A}, \mathbf{S})$ [cf., (1)], and simple model like this is known to be capable of improving the computational efficiency and algorithmic stability in the optimization area [31]. Note that this is particularly true especially when one adopts the alternating minimization (AM)

algorithm like in the tensor completion method [41], where fewer number of LFs is always preferred to reduce the local optimality effect in alternating optimization. Besides the physical interpretability, this is another motivation for us to adopt the simple 2-LF model (1), and, as another contribution, we will demonstrate that for the HTC problem, a model as concise as (1) (involving just two LFs) is sufficient for the tensor completion task.

Another two contributions are that the powerful JE topology in functional analysis is introduced into the tensor completion research for the first time, and that this powerful topology ensures a high-fidelity estimation of the first LF $\boldsymbol{A}$ allowing us to bypass the possibly time-consuming alternating optimization scheme (cf., Sections II-C and II-D). To understand the high effectiveness of the JE topology, we need to concisely recall three historical milestones in estimating the hyperspectral endmembers $\boldsymbol{A} = [\boldsymbol{a}_1, \ldots, \boldsymbol{a}_N]$.

For the first milestone, researchers assumed that the HSI has the highest data purity (i.e., the condition "$\gamma = 1$" mentioned in Section I), meaning that the pixel resolution is high enough such that there exists a pure pixel $[\mathbf{X}]_{\ell_1,\ell_2,:}$ containing just the ith material (i.e., $[\mathbf{X}]_{\ell_1,\ell_2,:} = \boldsymbol{a}_i$) for all i. This assumption is mathematically very convenient because it means that all $\boldsymbol{a}_i$'s already exist as some hyperspectral pixels in the considered HSI. That said, the estimation of $\boldsymbol{A}$ is simplified as a pixel search problem, inducing the seminal $\boldsymbol{A}$-estimation algorithm known as vertex component analysis (VCA) [49]. In general, the PPC criterion has the following mathematical form:

$$\mathcal{T}^\star \triangleq \arg\max_{\mathcal{T}\subseteq\mathcal{X}} \ \mathrm{vol}(\mathcal{T})$$

where $\mathrm{vol}(\cdot)$ denotes the volume operator, and $\mathcal{T}$ is a simplex contained in the data convex hull $\mathcal{X} \triangleq \mathrm{conv}\{[\mathbf{X}]_{\ell_1,\ell_2,:}|(\ell_1,\ell_2) \in \mathcal{I}_{L_1} \times \mathcal{I}_{L_2}\}$, from which one can prove that the vertices of the maximum-volume simplex $\mathcal{T}^\star$ are exactly the signature vectors $\{\boldsymbol{a}_1, \ldots, \boldsymbol{a}_N\}$ under the PPC $\gamma = 1$ [3], [34]. However, the PPC is often violated (especially in hyperspectral remote sensing), partly because the sensors are far away from the observed materials, and partly because lower spatial resolution should be used to compensate the high noise level caused by the high spectral resolution [50], leading to the second milestone based on the so-called CS criterion for estimating $\boldsymbol{A}$.

In CS, the data purity requirement is greatly reduced to "$\gamma > 1/\sqrt{N-1}$," as theoretically proved in [32], which is much milder than the pure pixel requirement "$\gamma = 1$." Specifically, the CS criterion turns to seek the minimum-volume simplex $\mathcal{T}$ containing the dataset $\mathcal{X}$, i.e.,

$$\mathcal{T}^\star \triangleq \arg\min_{\mathcal{X}\subseteq\mathcal{T}} \ \mathrm{vol}(\mathcal{T})$$

from which one can prove that the vertices of the minimum-volume simplex $\mathcal{T}^\star$ are exactly the signature vectors $\{\boldsymbol{a}_1, \ldots, \boldsymbol{a}_N\}$ whenever $\gamma > 1/\sqrt{N-1}$ [3], [34]. Though the CS criterion is theoretically sound, inducing several benchmark $\boldsymbol{A}$-estimation algorithms such as hyperplane-based CS identification (HyperCSI) [15], a serious issue is that the above optimization problem is actually a nonconvex NP-hard problem [51], preventing a simultaneously accurate and fast estimation process for $\boldsymbol{A}$.

The third milestone is hence motivated with research developments based on the JE criterion, defined in (2). JE also guarantees perfect recovery of $\boldsymbol{A}$ (cf., Lemma 1) by just requiring the same mild condition "$\gamma > 1/\sqrt{N-1}$" as the CS criterion—a beautiful coincidence! However, most beautifully, the JE criterion avoids the NP-hardness as it can be equivalently reformulated into a convex conic optimization problem that is polynomial-time solvable [34]. All in all, JE is the only criterion developed under the practical consideration of data purity without involving NP-hard computation burden. Though the high effectiveness of JE motivates us to apply it in our HTC theory, it was developed by assuming the availability of the full HSI tensor—another contribution of this article is then to solve this dilemma (cf., Section II-C) by extending the JE theory to address cases with incompletely observed HSI data, such that JE can be used to solve the HTC problem.

C. Recovery of the Endmember Matrix

This section aims at recovering the endmember matrix $\boldsymbol{A}$ from the incomplete HSI $\mathbf{X}_{\boldsymbol{\Omega}}$. To this end, we recall that JE has been theoretically and experimentally proved to be fundamental in hyperspectral analysis, as reported in recent machine learning literature [34]. In fact, JE has been applied to solve challenging inverse problems such as hyperspectral compressed sensing for metasurface-driven miniaturized satellite [52]. Simply speaking, JE is the maximum-volume ellipsoid inscribed in the data convex hull $\mathcal{X} \triangleq \mathrm{conv}\{[\mathbf{X}]_{\ell_1,\ell_2,:}|(\ell_1,\ell_2) \in \mathcal{I}_{L_1} \times \mathcal{I}_{L_2}\}$ [cf., the brown polytope in Fig. 1(b)]. To be precise, the computation of JE $\mathcal{E}^\star$ can be defined by the following optimization problem:

$$\mathcal{E}^\star \triangleq \arg\max_{\mathcal{E}\subseteq\mathcal{X}} \ \mathrm{vol}(\mathcal{E}) \tag{2}$$

where $\mathrm{vol}(\cdot)$ denotes the volume of a measurable set. Remarkably, using simple affine transform or simplex fitting [3], [34], the endmember matrix $\boldsymbol{A}$ can be perfectly recovered from $\mathcal{E}^\star$ under a rather mild sufficient condition, as detailed in the following lemma.

Lemma 1: If the number of materials $N \geq 3$ and the data purity $\gamma > 1/\sqrt{N-1}$, where

$$\gamma \triangleq \sup\{r \leq 1|(r\mathcal{B}_N) \cap \mathcal{T}_e \subseteq \mathcal{S}\} \tag{3}$$

in which $\mathcal{S} \triangleq \mathrm{conv}\{[\mathbf{S}]_{\ell_1,\ell_2,:}|(\ell_1,\ell_2) \in \mathcal{I}_{L_1} \times \mathcal{I}_{L_2}\} \subseteq \mathbb{R}^N$, $\mathcal{B}_N \triangleq \{\boldsymbol{x} \in \mathbb{R}^N | \|\boldsymbol{x}\|_2 \leq 1\}$ is the unit ball and $\mathcal{T}_e \triangleq \mathrm{conv}\{\boldsymbol{e}_1^{(N)}, \ldots, \boldsymbol{e}_N^{(N)}\} \subseteq \mathbb{R}^N$ is the unit simplex, then $\boldsymbol{A}$ can be perfectly recovered from $\mathcal{E}^\star$. □

To get a sense of Lemma 1, one can use the JE $\mathcal{E}^\star$ to generate an auxiliary matrix $\boldsymbol{Q} \in \mathbb{R}^{M\times N}$ and the $N \times N$ all-one matrix $\boldsymbol{\Psi}$ (detailed in Appendix), from which one can then compute the signatures as $\boldsymbol{A} = \boldsymbol{Q}\boldsymbol{\Psi} - (N-1)\boldsymbol{Q}$. This lemma is proven in Appendix, and it allows us to focus on the computation of the JE $\mathcal{E}^\star$ next.

Note that the computation of JE $\mathcal{E}^\star$ requires the information of the complete HSI tensor $\mathcal{X}$, as can be seen from (2). However, such information is lacking as we can just observe $\mathbf{X}_{\boldsymbol{\Omega}}$ in the HTC problem. Before solving this dilemma, we remark that the PPC $\gamma = 1$ is theoretically equivalent to the widely adopted separability assumption in machine learning [49], [53], comparing to which the sufficient condition $\gamma > 1/\sqrt{N-1}$ in Lemma 1 is rather mild especially for larger N, showing the great potential of the JE-based recovery of $\boldsymbol{A}$.

The remaining task of this section is to obtain JE, from which the estimate of $\boldsymbol{A}$ (denoted by $\widehat{\boldsymbol{A}}$) can be obtained,

as reported in Lemma 1. To this end, we just need to solve the aforementioned dilemma, based on another mild assumption

$$\text{(A1)} \quad \{m|(\ell_1,\ell_2,m)\in\mathbf{\Omega}\}\neq\emptyset \quad \forall(\ell_1,\ell_2)\in\mathcal{I}_{L_1}\times\mathcal{I}_{L_2}$$

meaning that each pixel in the HSI contains at least one observable band.

Since the dilemma originates from the lack of full information $\mathbf{X}$ required in (2), a natural solution is to roughly guess $\mathbf{X}$ from the observable data $\mathbf{X}_{\mathbf{\Omega}}$. We propose to have the rough guess of $\mathbf{X}$ as $\widetilde{\mathbf{X}}$, where

$$[\widetilde{\mathbf{X}}]_{\ell_1,\ell_2,m} \triangleq \begin{cases} [\mathbf{X}]_{\ell_1,\ell_2,m}, & \text{if } (\ell_1,\ell_2,m)\in\mathbf{\Omega} \\ [\mathbf{X}]_{\ell_1,\ell_2,f(\ell_1,\ell_2)}, & \text{if } (\ell_1,\ell_2,m)\notin\mathbf{\Omega},\ m<f(\ell_1,\ell_2) \\ [\mathbf{X}]_{\ell_1,\ell_2,g(\ell_1,\ell_2,m)}, & \text{if } (\ell_1,\ell_2,m)\notin\mathbf{\Omega},\ m>f(\ell_1,\ell_2) \end{cases} \tag{4}$$

in which $f(\ell_1,\ell_2)\triangleq\arg\min_b\{b|(\ell_1,\ell_2,b)\in\mathbf{\Omega}\}$ indicates the first observable band in the (ℓ_1,ℓ_2)th pixel, and $g(\ell_1,\ell_2,m)\triangleq\arg\max_b\{b<m|(\ell_1,\ell_2,b)\in\mathbf{\Omega}\}$ indicates the nearest previous observable band of the mth band in the (ℓ_1,ℓ_2)th pixel. We have the following remarks.

1) As the definition of f implies $(\ell_1,\ell_2,f(\ell_1,\ell_2))\in\mathbf{\Omega}$, the three cases in (4) have covered all the possibilities.
2) From the aforementioned assumption $\{m|(\ell_1,\ell_2,m)\in\mathbf{\Omega}\}\neq\emptyset$, one can ensure that both f and g exist and are uniquely defined, implying that the rough guess $\widetilde{\mathbf{X}}$ in (4) is well-defined.
3) The aforementioned (A1) is very mild and actually implied by another assumption (i.e., (A2), to be introduced later). Even though, we still keep adopting (A1) because this milder assumption is sufficient to guarantee the rough guess in (4) to be well-defined.

The rationale behind the definition of (4) is based on the observation of real HSI data. To be specific, inpainting those unobservable entries into $\widetilde{\mathbf{X}}$ by some nearest observable entries in $\mathbf{X}$ (cf., the definition of g) is quite natural because the real endmember signatures in the U.S. geological survey (USGS) library [54] are mostly continuous across spectral bands; this phenomenon is because the reflectances of a material are often similar for two nearby wavelengths. This observation implies that the data distribution of $\widetilde{\mathbf{X}}$ is similar to that of $\mathbf{X}$, in turn implying that the maximum-volume ellipsoids inscribed in the two data convex hulls (i.e., JEs) also remain almost the same, as graphically illustrated in Fig. 1. Therefore, the JE $\mathcal{E}^\star$ can be well-approximated by the following equation:

$$\widetilde{\mathcal{E}}^\star \triangleq \arg\max_{\mathcal{E}\subseteq\widetilde{\mathcal{X}}} \ \text{vol}(\mathcal{E}) \tag{5}$$

where $\widetilde{\mathcal{X}} \triangleq \text{conv}\{[\widetilde{\mathbf{X}}]_{\ell_1,\ell_2,:}|(\ell_1,\ell_2)\in\mathcal{I}_{L_1}\times\mathcal{I}_{L_2}\}$. The problem (5) is known to be a convex optimization problem and can be efficiently solved using the conic optimization theory [3], [34].

D. Recovery of the Abundance Tensor

This section aims at recovering the abundance tensor $\mathbf{S}$ from the observable data $\mathbf{X}_{\mathbf{\Omega}}$. Define the tensor Frobenius norm as $\|\mathbf{T}\|_{F,\mathbf{\Omega}}\triangleq\sqrt{\sum_{(\ell_1,\ell_2,m)\in\mathbf{\Omega}}[\mathbf{T}]^2_{\ell_1,\ell_2,m}}$. Then, a natural criterion for recovering the abundance tensor $\mathbf{S}$ is given by the following equation:

$$\widehat{\mathbf{S}}\triangleq\arg\min_{\mathbf{S}}\frac{1}{2}\left\|\mathbf{X}_{\mathbf{\Omega}}-\mathbf{S}\times_3\widehat{\boldsymbol{A}}\right\|^2_{F,\mathbf{\Omega}}+\iota_+(\mathbf{S}) \tag{6}$$

where ι_+ denotes the indicator function of the nonnegative orthant of the considered space (e.g., $\mathbb{R}^{L_1\times L_2\times N}$ here). In the criterion (6), the data-fitting term $\|\mathbf{X}_{\mathbf{\Omega}}-\mathbf{S}\times_3\widehat{\boldsymbol{A}}\|^2_{F,\mathbf{\Omega}}$ naturally comes from (1), while the regularizer $\iota_+(\cdot)$ comes from the nonnegativity of the abundances. Since both the data-fitting term and the regularizer are convex functions, the criterion (6) can be solved using the convex optimization theory as well.

To be precise, we first note that (6) can be decoupled with respect to the first two dimension of the tensor $\mathbf{S}$, i.e.,

$$\min_{[\mathbf{S}]_{\ell_1,\ell_2,:}}\frac{1}{2}\left\|\boldsymbol{x}_{\ell_1,\ell_2}-[\mathbf{S}]_{\ell_1,\ell_2,:}\times_3\widehat{\boldsymbol{A}}\right\|^2_{F,\mathbf{\Omega}}+\iota_+([\mathbf{S}]_{\ell_1,\ell_2,:}) \tag{7}$$

where $\boldsymbol{x}_{\ell_1,\ell_2}\triangleq[\mathbf{X}_{\mathbf{\Omega}}]_{\ell_1,\ell_2,:}$ with the support $\mathbf{\Omega}$ in (7) reduced to the (ℓ_1,ℓ_2)th pixel. As (7) is nothing but the well-known convex nonnegative least-squares (NNLS) problem, it can be efficiently solved by calling off-the-shelf NNLS solvers, such as "lsqnonneg" or "sunsal" in the typical numerical computing environment MATLAB [55]. Once $\widehat{\mathbf{S}}$ is obtained, it, together with $\widehat{\boldsymbol{A}}$ computed in Section II-C, can be used to reconstruct the full HSI by (1). Specifically, we have the inpainted image $\widehat{\mathbf{X}}=\widehat{\mathbf{S}}\times_3\widehat{\boldsymbol{A}}$.

We conclude this section by proposing a practical strategy of parallel computing to speed up the computation of abundance tensor, based on another assumption

$$\text{(A2)} \quad |\{m|(\ell_1,\ell_2,m)\in\mathbf{\Omega}\forall(\ell_1,\ell_2)\in\mathcal{I}_{L_1}\times\mathcal{I}_{L_2}\}|\geq N$$

where $|\cdot|$ denotes the set cardinality. For notational simplicity, we define as follows:

$$I_C\triangleq\{m|(\ell_1,\ell_2,m)\in\mathbf{\Omega}\forall(\ell_1,\ell_2)\in\mathcal{I}_{L_1}\times\mathcal{I}_{L_2}\} \tag{8}$$

which is the index set for the completely observed bands in (A2). The assumption (A2) means that there are at least N completely observed bands in $\mathbf{X}_{\mathbf{\Omega}}$, allowing us to simplify the criterion (6) as follows:

$$\widehat{\mathbf{S}}\triangleq\arg\min_{\mathbf{S}}\frac{1}{2}\left\|\mathring{\mathbf{X}}-\mathbf{S}\times_3\mathring{\boldsymbol{A}}\right\|^2_F+\iota_+(\mathbf{S}) \tag{9}$$

which not only computes all the $[\mathbf{S}]_{\ell_1,\ell_2,:}$ in parallel but avoids the unordinary norm $\|\cdot\|_{F,\mathbf{\Omega}}$ used in (6), where $\mathring{\boldsymbol{A}}$ is a submatrix of $\widehat{\boldsymbol{A}}$ formed by stacking those rows $[\widehat{\boldsymbol{A}}]_{m,:}$ with row indices in I_C, $\mathring{\mathbf{X}}$ is a subtensor of $\mathbf{X}_{\mathbf{\Omega}}$ formed by stacking those slices $[\mathbf{X}_{\mathbf{\Omega}}]_{:,:,m}$ with slice indices m in I_C, and the index set I_C is defined in (8). Theoretically, as (A2) ensures that just the data-fitting term of (9) itself has induced a well-posed criterion, one may further simplify (6) by removing the regularizer $\iota_+(\mathbf{S})$ from (6), leading to the closed-form recovery of $\widehat{\mathbf{S}}:=\mathring{\mathbf{X}}\times_3[(\mathring{\boldsymbol{A}}^{\mathrm{T}}\mathring{\boldsymbol{A}})^{-1}\mathring{\boldsymbol{A}}^{\mathrm{T}}]$. However, we empirically found that forcing the nonnegativity yields better recovery performance. Finally, we remark that (A2) is also a mild assumption because there are several hundreds of bands in real hyperspectral data, while we just need N (usually within ten) completely acquired spectral bands in $\mathbf{X}_{\mathbf{\Omega}}$.

The proposed parameter-tuning-free algorithm, referred to as functional analysis based convex HTC (FACHTC), is summarized in Algorithm 1, whose high efficacy will be experimentally illustrated in Section III.

III. Experimental Results

In this section, we will test the proposed FACHTC algorithm using both real and synthetic data. To be specific,

Algorithm 1 FACHTC Algorithm

1: **Given** incompletely observed HSI data $\mathbf{X}_{\mathbf{\Omega}}$.
2: Compute $\widetilde{\mathbf{X}}$ using (4).
3: Compute $\widetilde{\mathcal{E}}^{\star}$ from $\widetilde{\mathbf{X}}$ using (5).
4: Compute $\widehat{\boldsymbol{A}}$ from $\widetilde{\mathcal{E}}^{\star}$ using Lemma 1.
5: Compute $(\mathring{\boldsymbol{A}}, \mathring{\mathbf{X}})$ from $(\widehat{\boldsymbol{A}}, \mathbf{X}_{\mathbf{\Omega}})$.
6: Compute $\widehat{\mathbf{S}}$ from $(\mathring{\boldsymbol{A}}, \mathring{\mathbf{X}})$ using (9).
7: Compute $\widehat{\mathbf{X}} = \widehat{\mathbf{S}} \times_3 \widehat{\boldsymbol{A}}$ using (1).
8: **Output** the reconstructed full HSI tensor $\widehat{\mathbf{X}}$.

in Section III-A, we will test the performance of FACHTC on real hyperspectral data to assess the qualitative quality of the reconstructed HSI tensor. For fair comparison, in Section III-B, we will also investigate quantitative results to show the superiority of FACHTC when comparing to other benchmark HTC methods, including partial differential equation-based algorithm (PDE) [56], UBI [17], LRTV [13], KBRTC [21], FastHyIn [25], trace norm regularized CP decomposition method (TNCP) [38], alternating direction method-based tensor recovery (ADM-TR) [40], tensor completion by parallel matrix factorization via tensor train rank (TMac-TT) [44], tensor ring low-rank factors (TRLRF) [46], weighted low-rank tensor recovery model (WLRTR) [22], nonlocal-meets-global restoration paradigm (NGmeet) [47], tensor nuclear norm model with discrete cosine transform (TNN-DCT) [43], and multi-mode deep matrix and tensor factorization (M2DMTF) [57]. Among these methods, only UBI does not require the user to prespecify the location of missing data in $\overline{\mathbf{\Omega}}$, and, in this regard, this unmixing-based approach is friendly. Finally, in Section III-C, we will show that when applying the proposed FACHTC method to reconstruct the HSI data, the classification result performed on the recovered data also yields the best classification accuracy in comparison to other HTC methods.

A. Qualitative Analysis

In this section, we investigate the HTC performance of the proposed FACHTC algorithm, as well as 12 benchmark peer methods, using real hyperspectral data. For real data experiments, we just have incompletely acquired HSI tensor, meaning that there is no ground-truth HSI for quantitative evaluation, and thus we will focus on the visual quality assessment on the reconstructed HSI using various HTC methods. The studied HSI data are acquired by the Hyperion push-broom type Earth Observing-1 (EO-1) satellite launched by National Aeronautics and Space Administration (NASA). The region of interest (ROI) is situated in Odisha state, located in the northeastern part of India; this ROI contains 400×200 pixels, as displayed in Fig. 2(a) [58]. After removing atmospheric water vapor bands, a total of 117 spectral bands are used in this experimental study.

The 103rd band of this testing HSI contains a dead line running through the entire band image, as shown in Fig. 2(b). The dead line is inpainted using PDE, UBI, LRTV, KBRTC, FastHyIn, TNCP, ADM-TR, TMac-TT, TRLRF, WLRTR, NGmeet, TNN-DCT, M2DMTF, as well as the proposed FACHTC, and the reconstructed images are, respectively, shown in Fig. 2(c)–(p). As the single dead line does not pose a complicated inpainting scenario, one can see that all the methods under test have recovered the corrupted area. The band image reconstructed by LRTV shows some luminance aberration, as can be seen from Fig. 2(e). As for the other 12 peer methods (i.e., PDE, UBI, KBRTC, FastHyIn, TNCP, ADM-TR, TMac-TT, TRLRF, WLRTR, NGmeet, TNN-DCT, M2DMTF) and the proposed FACHTC, the reconstructed band images all show pleasant visual results, as displayed in Fig. 2(c), (d), and (f)–(p).

Next, we test a more challenging case using the 35th band of the testing HSI, whose left region is seriously corrupted by densely populated stripes, as shown in Fig. 3(a). Similar stripe corruptions are also observed in the same areas of bands 33 and 34. The corresponding mask $\overline{\mathbf{\Omega}}$ covering the corrupted region is shown in Fig. 3(b), which is obtained based on the following practical concerns. As discussed in the beginning of Section II, it is not friendly to require the exact mask information especially when the missing entries are densely populated like Fig. 3(a). Furthermore, the quality of pixels lying between two very close stripes is unreliable, because, from some most commonly adopted hyperspectral imaging models (e.g., Gaussian kernel modeling [59]), one can see that the imaging quality is directly affected by the neighboring pixels. In other words, when the damaged stripes are densely populated [e.g., Fig. 3(a)], the pixels in between could be of very low quality. Thus, we opt not to use the unreliable information, leading to the mask shown in Fig. 3(b). Automatically identifying high-quality pixels to form the mask $\overline{\mathbf{\Omega}}$ is a challenging but valuable future work.

Various HTC methods are used to reconstruct the image with the results shown in Fig. 3(c)–(p). Since PDE uses neighboring information to inpaint the image, it fails to recover such a large area corruption, as can be seen from Fig. 3(c). The image recovered by LRTV, displayed in Fig. 3(e), again shows luminance distortion. Apart from PDE and LRTV, the results of TNCP, ADM-TR, TMac-TT, and WLRTR suffer from different degrees of local blurring in the recovered region. The image recovered by KBRTC, displayed in Fig. 3(f), shows nice qualitative result for the real scenario of large spatial corruptions simultaneously occurring in consecutive bands. As for UBI, FastHyIn, TRLRF, NGmeet, TNN-DCT, M2DMTF, and the proposed FACHTC, the reconstructed images also yield nice qualitative results, as can be observed from Fig. 3(d), (g), (k), and (m)–(p). It is interesting to note that though M2DMTF is not customized for hyperspectral tensor, it yields good qualitative result. To further understand the superiority of FACHTC, over UBI, KBRTC, FastHyIn, TRLRF, NGmeet, TNN-DCT, and M2DMTF, we need to perform quantitative evaluation next.

B. Quantitative Analysis

To fairly compare the proposed FACHTC algorithm with other benchmark HTC methods, we need quantitative analysis based on standard performance metrics, including peak signal-to-noise ratio (PSNR), universal image quality index (UIQI), *erreur relative globale adimensionnelle de synthèse* (ERGAS), spectral angle mapper (SAM), and structural similarity (SSIM) [50], [60], [61], [62], [63], [64]. Higher value of PSNR indicates a better HTC performance. The upper bound of UIQI is achieved if and only if the perfect reconstruction is achieved. ERGAS measures global reconstruction quality; the smaller the value of ERGAS, the higher the global quality of the reconstructed HSI. SAM measures the spectral angle error; the smaller the value of SAM, the better the spectral quality of the reconstructed HSI. SSIM is an index designed based on

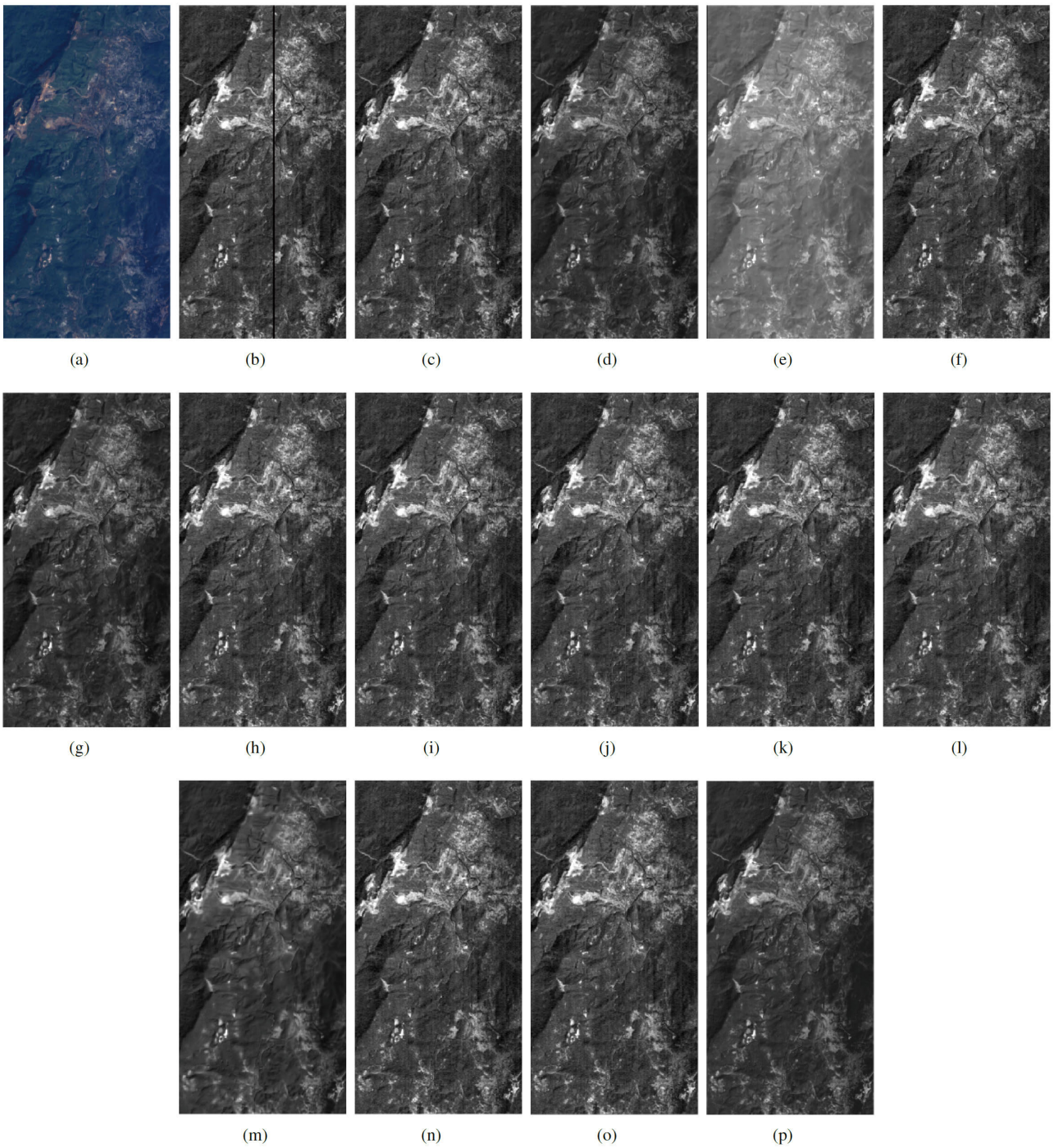

Fig. 2. (a) Color composition (R: 29, G: 23, B: 16) of the studied ROI in the Odisha data. (b) 103th band of this real testing data is corrupted by a dead line. The image is reconstructed using (c) PDE, (d) UBI, (e) LRTV, (f) KBRTC, (g) FastHyIn, (h) TNCP, (i) ADM-TR, (j) TMac-TT, (k) TRLRF, (l) WLRTR, (m) NGmeet, (n) TNN-DCT, (o) M2DMTF and (p) proposed FACHTC.

human vision, accounting for loss of correlation, luminance distortion, and contrast distortion, respectively; higher value of SSIM indicates a better HTC performance. The following experiments are executed on a computer facility equipped with Core-i7-9750H CPU with 2.60-GHz speed and 32-GB RAM, and all the HTC methods under test are implemented in MathWorks MATLAB R2019a. Accordingly, the computational time T in second (sec.) will also be used to evaluate the computational efficiency.

The reference image is acquired by the Hyperspectral digital imagery collection experiment (HYDICE) sensor, and it is collected over the Washington DC Mall by Spectral Information Technology Application Center of Virginia (SITAC) [25], [65]. The false-color composition of the 256 $\times$ 256 reference image is shown in Fig. 4. We consider a challenging scenario, for which, among a total of 191 spectral bands, there are 176 seriously corrupted bands, including bands 6–100 and bands 106–186. The corruptions on the 176 bands are in the same region resulting in severe disruption of spectral continuity when forming the identifiable material hyperspectral signatures, preventing the computation of valid inpainting quantities from adjacent elements of the

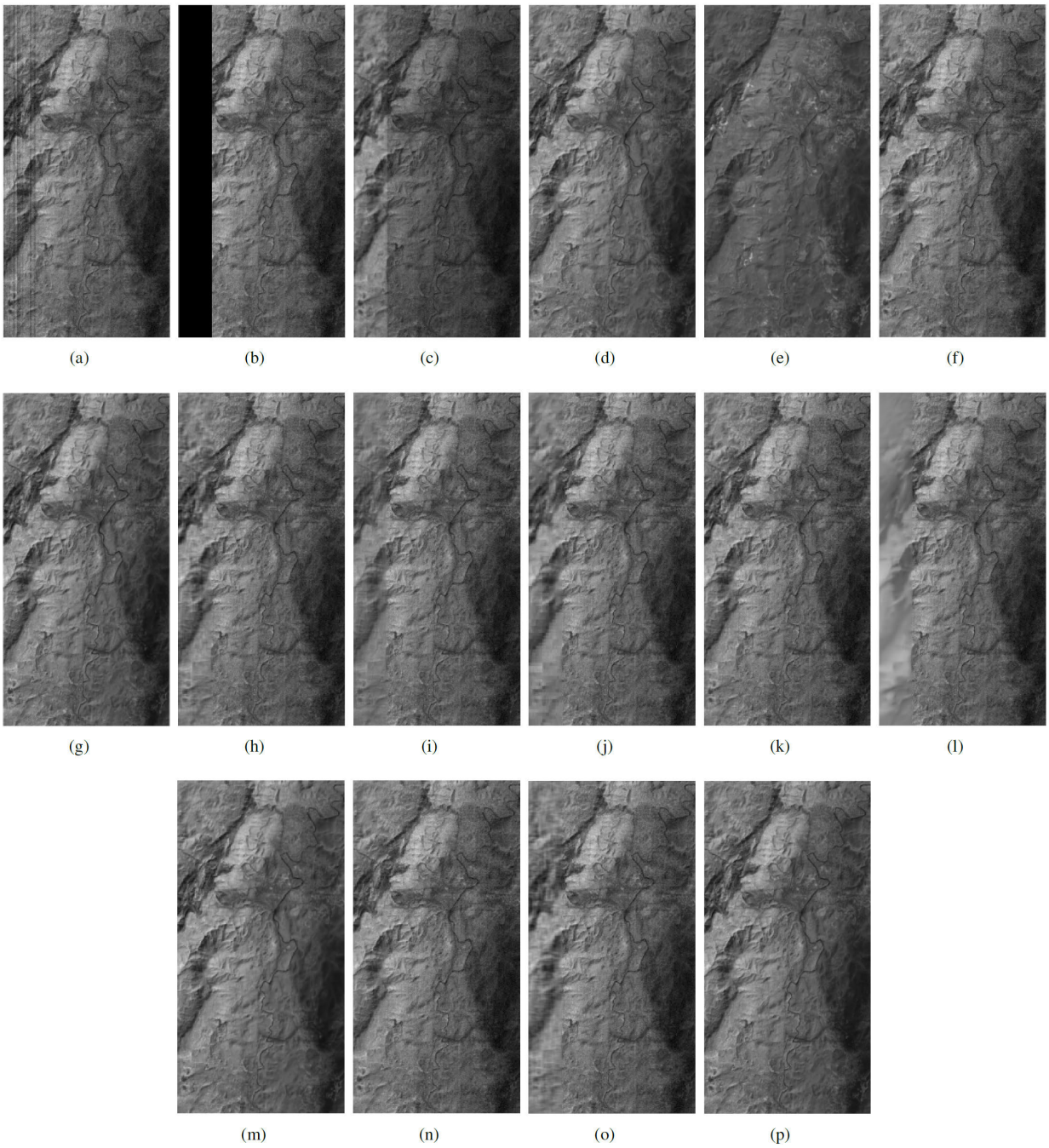

Fig. 3. (a) 35th band of the real testing Odisha data is corrupted by densely populated stripes, for which the corresponding mask $\overline{\mathbf{\Omega}}$ covering the corrupted region is shown in subfigure (b). The image is reconstructed using (c) PDE, (d) UBI, (e) LRTV, (f) KBRTC, (g) FastHyIn, (h) TNCP, (i) ADM-TR, (j) TMac-TT, (k) TRLRF, (l) WLRTR, (m) NGmeet, (n) TNN-DCT, (o) M2DMTF and (p) proposed FACHTC.

HSI tensor. The 20th band of the clean image and its corruption pattern are shown in Fig. 6(a) and (b), respectively. Then, this highly damaged HSI tensor is reconstructed by PDE [56], UBI [17], LRTV [13], KBRTC [21], FastHyIn [25], TNCP [38], ADM-TR [40], TMac-TT [44], TRLRF [46], WLRTR [22], NGmeet [47], TNN-DCT [43], M2DMTF [57], and the proposed FACHTC algorithm. Their quantitative performances are summarized in Table I, where the boldfaced number indicates the best performance with respect to a particular index.

From Table I, one can see that the proposed FACHTC achieves the state-of-the-art HTC performance in terms of all the four indices. Specifically, the PSNR measure indicates the spatial reconstruction quality, for which FACHTC, TNN-DCT, and FastHyIn are outstanding; among the 13 peer methods, the very recently developed M2DMTF achieves the best PSNR. For indices of UIQI and SSIM, the tensor/matrix factorization-based methods, i.e., FACHTC, UBI, TNN-DCT, and M2DMTF, are highly competitive. The proposed FACHTC has the best global reconstruction quality, as indicated by the ERGAS measure. Finally, for hyperspectral applications, preserving the spectral shape during the processing procedure is important for the subsequent tasks (e.g., classification; cf., Section III-C). With this regard, the most important measure would be SAM, in terms of which the proposed FACHTC again yields the best performance, while M2DMTF has best spectral reconstruction quality among the other 13 peer methods. Finally, FastHyIn is fastest among the

Fig. 4. False-color composition (R: 60, G: 27, B: 17) of the studied ROI in the Washington DC Mall data.

TABLE I

QUANTITATIVE COMPARISON BETWEEN THE PROPOSED FACHTC ALGORITHM AND OTHER BENCHMARK HTC METHODS

	PSNR	UIQI	ERGAS	SAM	SSIM	T (sec.)
PDE	26.24	0.828	71.06	2.795	0.912	594.0
UBI	26.71	0.922	23.15	2.118	0.950	16.58
LRTV	13.64	0.425	2887	6.732	0.450	95.61
KBRTC	26.737	0.860	25.62	4.449	0.899	671.5
FastHyIn	28.38	0.837	36.87	9.196	0.880	**6.890**
TNCP	22.19	0.730	65.57	15.04	0.800	85.00
ADM-TR	22.62	0.758	57.41	4.719	0.836	8327
TMac-TT	28.21	0.889	22.51	2.740	0.939	216.4
TRLRF	20.98	0.635	227.5	4.369	0.841	2391
WLRTR	27.82	0.881	22.45	2.388	0.937	1472
NGmeet	22.23	0.752	38.14	6.996	0.827	40.57
TNN-DCT	29.24	0.909	19.89	2.233	0.948	288.2
M2DMTF	29.27	0.915	24.25	2.072	0.965	1038
FACHTC	**32.27**	**0.959**	**14.687**	**1.553**	**0.969**	7.610

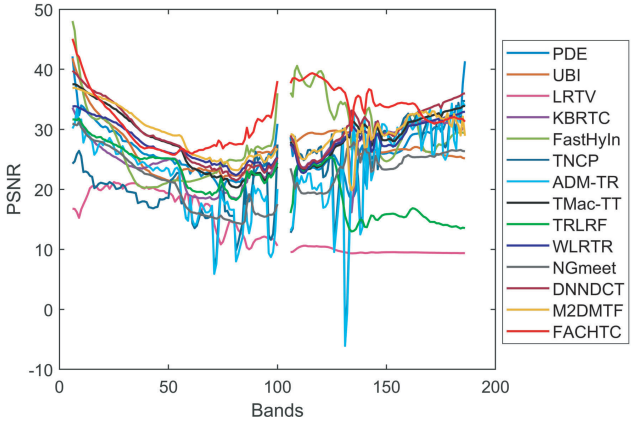

Fig. 5. Band-by-band analysis for the proposed FACHTC algorithm and other benchmark HTC methods.

methods under investigation, while FACHTC has nearly the same computational efficiency.

To have deeper understanding, we further show the visual comparison in Fig. 6, the band-by-band analysis in Fig. 5, and the LF analysis in Fig. 7. As can be seen from Fig. 6(c), (e), and (l), PDE, LRTV, and WLRTR completely fail to reconstruct the HSI tensor for this challenging scenario. KBRTC, FastHyIn, TNCP, ADM-TR, TRLRF, and NGmeet induce strong local noise and shadow aliasing artifact in the reconstructed image, as can be observed in Fig. 6(f)–(i), (k), and (m). Furthermore, TMac-TT and TNN-DCT achieve relatively acceptable visual results, but still suffer from slight distortion in the recovered large missing regions, as can be seen from Fig. 6(j) and (n). Only UBI, M2DMTF, and FACHTC perform well in this scenario, as alluded by Fig. 6(d), (o), and (p), well aligning with the quantitative analysis presented in Table I. However, the superiority of FACHTC over UBI will be seen in the subsequent applications; cf., Section III-C. To show that the proposed FACHTC algorithm has uniformly good performance across different spectral bands, the band-by-band PSNR values of the reconstructed bands 6–100 and bands 106–186 are plotted in Fig. 5, where one can see that FACHTC does yield best performances for bands 55–170 and nearly the best performances also for the other bands.

Since we have ground truth for the synthetic data, we can go a step further to explain the good performance of FACHTC by investigating its LFs, i.e., $(\widehat{\boldsymbol{A}}, \widehat{\mathbf{S}})$, which are shown in Fig. 7. The $N = 7$ columns of the endmember matrix $\widehat{\boldsymbol{A}}$ are shown in the upper part of Fig. 7, and the corresponding 2-D slices of the 3-D abundance tensor $\widehat{\mathbf{S}}$ are shown in the lower part of Fig. 7. As alluded by Fig. 1, the data convex hull $\mathcal{X}$ remains almost unchanged even with a large percentage of missing data. By (2) and Lemma 1, a direct theoretical consequence is then that the estimated endmembers also remain almost the same. So, the good performance of FACHTC is expected. To experimentally verify this point, we compute the endmembers via FACHTC but directly from the ground-truth data (i.e., uncorrupted data), and the results are also shown in the upper part of Fig. 7. One can see that the LF $\widehat{\boldsymbol{A}}$ does hold high resemblance to the ground-truth ones, double confirming the state-of-the-art performance of FACHTC. The superiority of FACHTC directly contributes to the subsequent HSI applications, as will be illustrated in the next section.

C. Application of FACHTC to Land Cover Classification

Besides quantitative analysis, another straightforward way to evaluate the quality of the reconstructed HSI tensor is to test the classification performance based on the reconstructed hyperspectral signatures [66]. As aforementioned, hyperspectral data play an irreplaceable role in remote material identification as its complete spectral information allows depicting unique material signatures for different materials. This property facilitates the classification accuracy when comparing to other imageries. However, when the HSI is incompletely observed, the spectral signature information is also lacking, making the classification task intractable. In this experiment, we apply the proposed FACHTC algorithm to reconstruct the full HSI tensor and show that the classification performed on the material signatures reconstructed by FACHTC does yield best accuracy when comparing to other benchmark HTC methods.

To evaluate the classification performance, we need some standard indices, including overall accuracy (OA) [67], average accuracy (AA) [68], and kappa statistics (κ) [69]. The κ further removes the effect caused by a "random-guessing algorithm" yielding correct classification results. Higher values of OA, AA, and κ indicate better classification performances.

The testing data are acquired by the reflective optics system imaging spectrometer (ROSIS) sensor over a 570 × 300 ROI on the Pavia University, northern Italy [70], as illustrated in Fig. 8(a). These data have a high spatial resolution of 1.3 m and are thus suitable for evaluating the classification

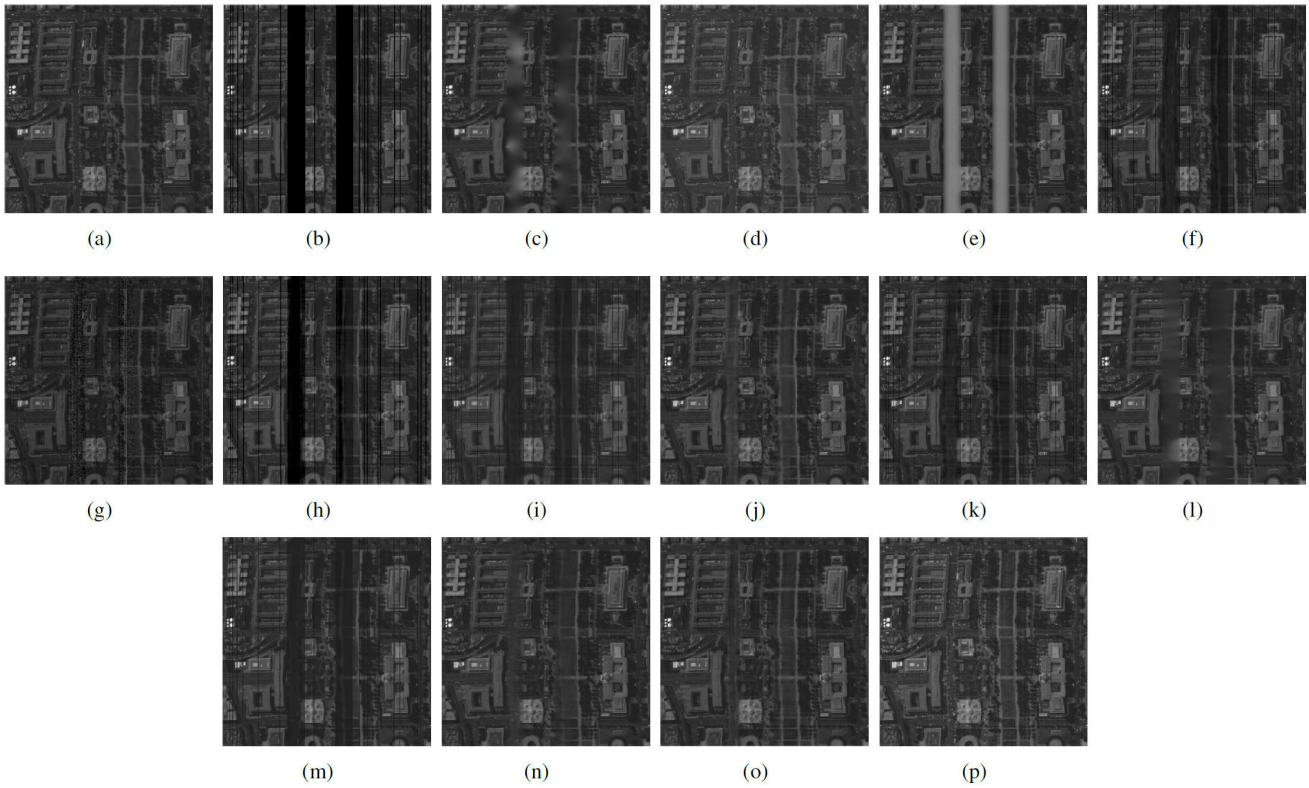

Fig. 6. (a) 20th band of the reference image of the Washington DC Mall data. (b) Seriously corrupted image indicates a challenging HTC scenario. The image reconstructed by (c) PDE, (d) UBI, (e) LRTV, (f) KBRTC, (g) FastHyIn, (h) TNCP, (i) ADM-TR, (j) TMac-TT, (k) TRLRF, (l) WLRTR, (m) NGmeet, (n) TNN-DCT, (o) M2DMTF, and (p) proposed FACHTC.

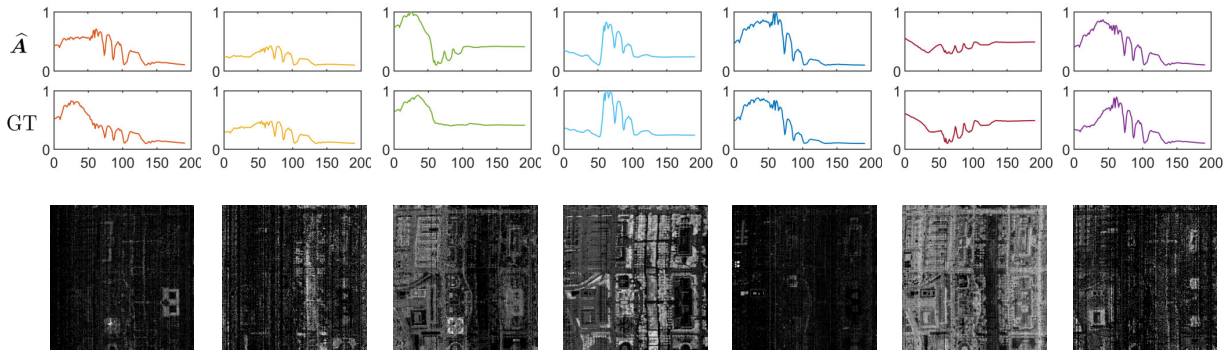

Fig. 7. In the upper part of this figure, we show the columns of the LF $\widehat{\boldsymbol{A}} \in \mathbb{R}^{191\times 7}$ (i.e., endmember matrix), together with its counterpart directly computed from the ground-truth (GT) data. The 2-D slices of the 3-D LF $\widehat{\mathcal{S}} \in \mathbb{R}^{256\times 256\times 7}$ (i.e., abundance tensor) are displayed in the lower part. The high resemblance between $\widehat{\boldsymbol{A}}$ and the GT ones explains the good performance of FACHTC.

performance. There are nine classes (i.e., Asphalt, Meadows, Gravel, Trees, Metal Sheets, Bare Soil, Bitumen, Bricks, and Shadows) with the ground-truth classification survey summarized in Table II and Fig. 9(a); cf., the land cover classes (and the corresponding number of pixels in each class) reported in [65]. The studied image, containing 103 spectral bands, is seriously corrupted, and the corruption appears in contiguous bands 21–60 with the pattern displayed in Fig. 8(b). These data are reconstructed using various HTC methods (i.e., PDE, UBI, LRTV, KBRTC, FastHyIn, TNCP, ADM-TR, TMac-TT, TRLRF, WLRTR, NGmeet, TNN-DCT, M2DMTF [57]) and the proposed FACHTC method, followed by feeding the reconstructed HSI into a benchmark deep classifier [71] to obtain the classification maps. To be more specific, the used deep classifier is based on the 3-D convolutional neural network for joint spectral–spatial feature extractions [71]. The classifier [71] requires just limited training samples from the original HSI; specifically, just 50% labeled samples (training set) of the Pavia University data are used during the training phase, and, among the training set, 5% of the samples are used for validation to avoid overfitting. The classifier [71] is trained using the original HSI, rather than the restored HSI, because if we use HSI restored by some HTC method, the learned statistics will be stitched to that method, unfair to other HTC methods. Note that this classification experiment is commonly used to further evaluate the performances of the HTC methods [72]. The obtained classification maps, corresponding to different HTC methods under test, are displayed in Fig. 9(b)–(o).

In the central bare soil region, there are many misclassified pixels in the maps of PDE, LRTV, FastHyIn, TNCP, ADM-TR, TMac-TT, TRLRF, WLRTR, NGmeet, TNN-DCT,

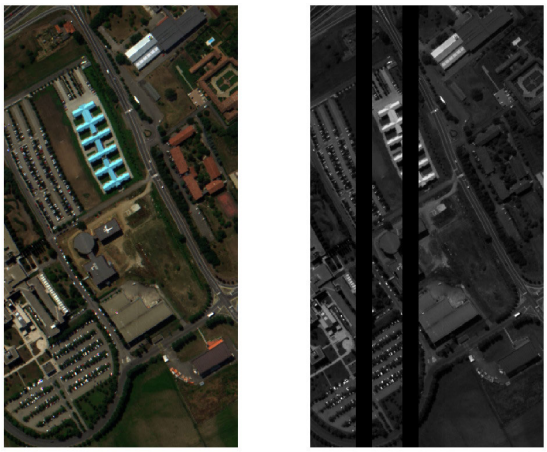

(a) (b)

Fig. 8. (a) False-color composition (R: 56, G: 33, B: 13) of the studied ROI in the Pavia University data. (b) Corrupted 30th band image.

TABLE II

LAND COVER CLASSES AND NUMBERS OF PIXELS ON THE UNIVERSITY OF PAVIA DATASET [65], [71]

NO.	Color	Class	Sample
1		Asphalt	5411
2		Meadows	12649
3		Gravel	1270
4		Trees	2694
5		Metal Sheets	1345
6		Bare Soil	5029
7		Bitumen	1330
8		Bricks	3616
9		Shadows	898

and M2DMTF, as can be seen from Fig. 9(b), (d), (f)–(j), and (l)–(n). For KBRTC and WLRTR, there are also a few misclassified pixels in the central part, as shown in Fig. 9(e) and (k). One can also see that some pixels belonging to the asphalt and trees categories are also misclassified in the classification map of KBRTC. According to the previous qualitative and quantitative evaluations, UBI is regarded as a strong competitor among the existing benchmark methods. However, when considering this classification application, UBI does not perform well in the upper left region and the lower central region, as can be seen from those misclassified pixels in Fig. 9(c). TMac-TT is also a strong peer method with outstanding HTC performances (cf., Table I), but, unlike the proposed FACHTC, the low-rank modeling adopted in TMac-TT is not customized based on the nature of HSI [cf., (1)], making the recovered hyperspectral signatures not suitable for the classification task [cf., Fig. 9(i)]. Similar comments are applicable to quite several other typical CP-based modelings as well. For the proposed FACHTC algorithm, though a few meadows pixels are misclassified, the generated classification map does show the best classification performance, as can be seen from Fig. 9(o). To fairly evaluate the classification performance, we display the values of OA, AA, and κ, as shown in Table III. As can be clearly seen, classification performed based on the HSI reconstructed using the proposed FACHTC algorithm does yield best accuracy, in terms of all the three indices. The successful application

TABLE III

QUANTITATIVE ANALYSIS OF THE CLASSIFICATION RESULTS BASED ON THE IMAGES RECONSTRUCTED BY BENCHMARK HTC METHODS AND FACHTC

	OA (%)	AA (%)	κ
PDE	86.39	80.56	0.825
UBI	91.72	85.30	0.897
LRTV	84.26	73.53	0.797
KBRTC	99.49	99.31	0.994
FastHyIn	98.81	98.35	0.985
TNCP	86.86	83.33	0.832
ADM-TR	94.76	92.08	0.934
TMac-TT	88.32	86.10	0.850
TRLRF	90.53	91.22	0.879
WLRTR	99.19	98.72	0.990
NGmeet	93.08	89.67	0.912
TNN-DCT	98.50	98.38	0.981
M2DMTF	92.75	92.23	0.907
FACHTC	**99.57**	**99.64**	**0.995**

TABLE IV

QUANTITATIVE COMPARISON BETWEEN FACHTC AND OTHER BENCHMARK HTC METHODS USING SOPHISTICATED MIXED CORRUPTIONS INVOLVING RANDOM MISSING PATTERNS

	PSNR	UIQI	ERGAS	SAM	SSIM	T (sec.)
PDE	18.41	0.324	5253	44.80	0.356	6633
LRTV	13.64	0.425	2887	6.732	0.450	95.61
KBRTC	30.22	0.908	21.91	5.117	0.934	840.5
TNCP	19.84	0.605	440.3	17.08	0.803	91.25
ADM-TR	19.95	0.684	62.92	12.02	0.824	8210
TMac-TT	26.85	0.803	32.94	4.887	0.886	240.4
TRLRF	22.28	0.611	470.7	7.612	0.794	1301
WLRTR	27.90	0.858	84.75	6.650	0.938	1388
NGmeet	31.09	0.964	14.91	3.574	0.982	48.32
TNN-DCT	31.860	0.933	17.617	**2.844**	0.961	303.3
M2DMTF	27.961	0.877	39.392	5.911	0.962	901.6
FACHTC	**32.285**	**0.969**	**13.730**	3.101	**0.984**	**11.02**

of FACHTC to the land cover classification double confirms its superiority in terms of both qualitative and quantitative analysis results.

D. HTC for Patterns Involving Random Missing

In this experiment, we further consider the random missing patterns. However, as our target application is for remote sensing, we would like to remark that stripe missing patterns are more commonly observed in real hyperspectral data (cf., NASA's real satellite data in Fig. 2) [14], [58]. To see it, considering the most commonly seen hyperspectral push-broom imaging system, if a sensor in the sensor array is aging or broken, those pixels on the trajectory the aging/broken sensor flies through will not be well-acquired, leading to missing patterns shaped like stripes/lines (rather than randomly scattered points). On the other hand, strip missing patterns are considered more challenging than random missing patterns; for example, considering a missing pixel (say, $\boldsymbol{x}$) in the wide stripe region of the band image displayed in Fig. 6(b), its eight neighboring pixels are all missing, while there would still have around four neighboring pixels (assuming the tough case of half random missing) to provide crucial information to recover $\boldsymbol{x}$. Even though random missing patterns may also happen if some entries of the HSI tensor were lost during the transmission from the satellite to the ground station.

Thus, besides the most commonly seen stripe patterns, this experiment further considers the random missing patterns

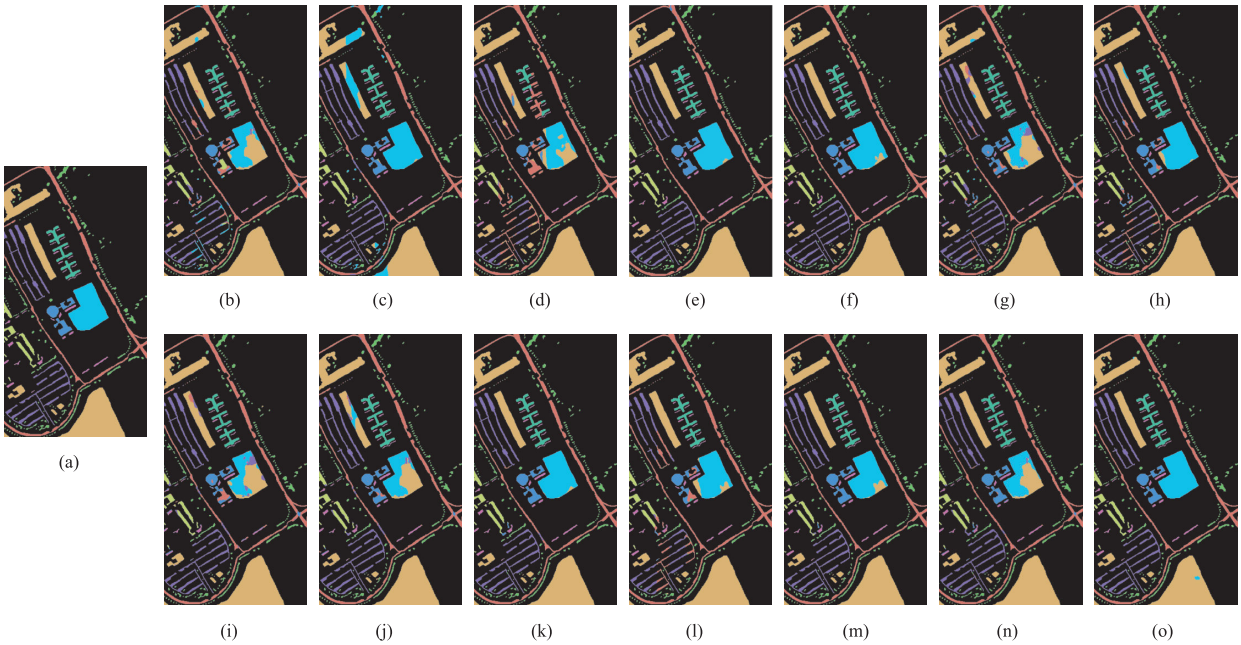

Fig. 9. (a) Classification ground truth of the studied Pavia University data. Classification maps using images recovered by (b) PDE, (c) UBI, (d) LRTV, (e) KBRTC, (f) FastHyIn, (g) TNCP, (h) ADM-TR, (i) TMac-TT, (j) TRLRF, (k) WLRTR, (l) NGmeet, (m) TNN-DCT, (n) M2DMTF, and (o) proposed FACHTC.

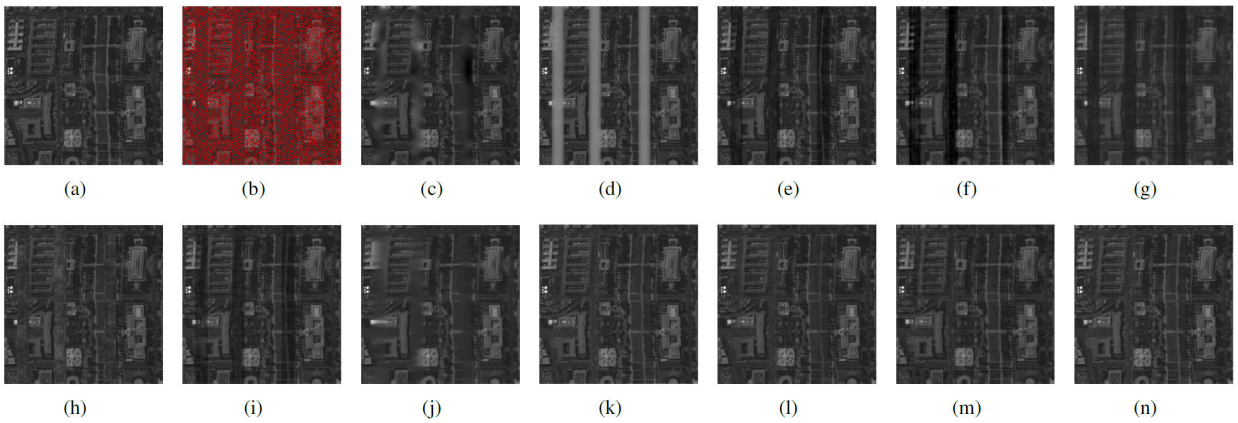

Fig. 10. (a) 20th band of the reference image of the Washington DC Mall data. (b) Seriously corrupted image indicates a challenging HTC scenario with sophisticated mixed corruptions, where red dots indicate the locations of random missing pixels. HTC results obtained from (c) PDE, (d) LRTV, (e) KBRTC, (f) TNCP, (g) ADM-TR, (h) TMac-TT, (i) TRLRF, (j) WLRTR, (k) NGmeet, (l) TNN-DCT, (m) M2DMTF, and (n) proposed FACHTC.

displayed in Fig. 10(b), where red dots denote the 40% random missing pixels. This is a sophisticated pattern mixed with random missing damages and large spatial–spectral corruptions (in spectral bands/rows 11–100 and 110–191, and spatial areas/columns 21–40, 81–100, and 161–180), which are simultaneously imposed on the HYDICE reference image [cf., Fig. 10(a)] collected over the Washington DC Mall [25], [65]. Theoretically, there is no constraint posed on the missing pattern $\boldsymbol{\Omega}$ when using FACHTC, as long as $\boldsymbol{\Omega}$ satisfies Assumptions (A1) and (A2). This will also be experimentally verified, as discussed below.

The quantitative results are summarized in Table IV with the qualitative results presented in Fig. 10. As can be seen from Fig. 10, only NGmeet, TNN-DCT, M2DMTF, and FACHTC have successfully recovered the structures for this seriously damaged hyperspectral tensor, and this observation well echos the best SSIM values of these methods in Table IV. To further evaluate the effectiveness of these three methods, we refer to Table IV. One can observe that the proposed FACHTC achieves best performances in terms of PSNR, UIQI, ERGAS, and SSIM, and nearly the best performance in terms of SAM. We remark that UBI and FastHyIn completely fail to deal with this highly damaged case returning error messages during the testing phase (so their results are not displayed), and that we divide the HSI tensor into three subtensors along the spectral dimension when testing PDE to mitigate its huge memory demand induced by the studied challenging missing pattern. This challenging scenario also leads to very slow computational speed for several methods under test. As can be seen from Table IV, FACHTC is the fastest algorithm. In fact, comparing to the second fastest method, i.e., NGmeet, the proposed FACHTC costs just about 20% computational time. All in all, thanks to the convexity of the adopted JE theory, our FACHTC algorithm again achieves the state-of-the-art performances in terms of both recovery accuracy and computational efficiency.

IV. Conclusion

We have presented an unsupervised HTC algorithm, termed FACHTC, for reconstructing incompletely observed

hyperspectral tensor. Since JE in functional analysis has revealed its fundamental role in hyperspectral data analysis, as reported in recent machine learning literature, FACHTC reconstructs the full hyperspectral tensor by customizing a convex JE-based criterion particularly for the HTC problem, followed by implementing the convex criterion. Thanks to the convexity of the adopted JE theory, our FACHTC algorithm achieves the state-of-the-art performances in terms of both recovery accuracy and computational efficiency. As HSI is distinguished by its capability of spectrum-based material identification, another straightforward way to evaluate the quality of the reconstructed HSI tensor is to test the corresponding classification efficacy. Therefore, we also proved that the land cover classification task conducted using the FACHTC-reconstructed data also yields outstanding classification accuracy. Finally, among the 13 methods under test (cf., Table I), only UBI and NGmeet can blindly infer the missing pattern $\boldsymbol{\Omega}$ at the cost of lower HTC performance. Extending FACHTC to such a fully blind setting without performance degradation is a challenging but highly valuable future research line.

APPENDIX
PROOF OF LEMMA 1

We just need to show the details of how to use the information embedded in JE $\mathcal{E}^\star$ to reconstruct the hyperspectral signatures $\boldsymbol{A}$. First, any ellipsoid can be obtained by affinely transforming the unit Euclidean ℓ_2-norm ball. Clearly, the JE is of dimension $N-1$, and thus the above-mentioned unit Euclidean ℓ_2-norm ball is also of dimension $N-1$. Therefore, the JE can be explicitly written as the affine mapping of the unit ball $\mathcal{B}_{N-1} \triangleq \{\boldsymbol{\alpha} \in \mathbb{R}^{N-1} \,|\, \|\boldsymbol{\alpha}\|_2 \leq 1\}$; to be specific, there are some full column rank $\boldsymbol{F} \in \mathbb{R}^{M\times(N-1)}$ and $\boldsymbol{c} \in \mathbb{R}^M$ such that

$$\mathcal{E}^\star \equiv \mathcal{E}^\star(\boldsymbol{F}, \boldsymbol{c}) \triangleq \{\boldsymbol{F}\boldsymbol{\alpha} + \boldsymbol{c} \,|\, \|\boldsymbol{\alpha}\|_2 \leq 1\}.$$

By [3, Th. 3], as long as $N \geq 3$ and $\gamma > 1/\sqrt{N-1}$, we can further see the relation between JE and the signatures, i.e.,

$$\begin{aligned} \boldsymbol{F} &= \left(1/\sqrt{N(N-1)}\right)\boldsymbol{A}\boldsymbol{C} \\ \boldsymbol{c} &= (1/N)\boldsymbol{A}\mathbf{1}_N \end{aligned}$$

where $\boldsymbol{C} \in \mathbb{R}^{N\times(N-1)}$ is any semi-unitary matrix satisfying $\boldsymbol{C}^{\mathrm{T}}\mathbf{1} = \mathbf{0}$. As proved in [3, Th. 3], from the data boundary $\bar{\mathcal{X}}$, i.e., the relative boundary of $\mathcal{X}$, one can obtain the so-called contact points $\boldsymbol{q}_1, \ldots, \boldsymbol{q}_N$ using $\{\boldsymbol{q}_1, \ldots, \boldsymbol{q}_N\} \triangleq \mathcal{E}^\star(\boldsymbol{F}, \boldsymbol{c}) \cap \bar{\mathcal{X}} \subseteq \mathbb{R}^M$. By [3, eq. (3.5)], we know that these contact points are highly related to the signatures $\boldsymbol{A}$, with an explicit relation given by the following equation:

$$\boldsymbol{q}_i = \frac{\boldsymbol{A}\left(\mathbf{1}_N - \boldsymbol{e}_i^{(N)}\right)}{N-1}, \quad i = 1, \ldots, N \tag{10}$$

if $N \geq 3$ and $\gamma > 1/\sqrt{N-1}$ are true. As a direct consequence of (10), the signatures $\boldsymbol{A} = [\boldsymbol{a}_1, \ldots, \boldsymbol{a}_N]$ can be obtained by the following equation:

$$\boldsymbol{A} = \boldsymbol{Q}\boldsymbol{\Psi} - (N-1)\,\boldsymbol{Q}$$

where $\boldsymbol{Q} = [\boldsymbol{q}_1, \ldots, \boldsymbol{q}_N]$ and $\boldsymbol{\Psi}$ is the $N \times N$ all-one matrix. Therefore, the proof has been completed. ■

REFERENCES

[1] J. Xue, Y. Zhao, W. Liao, J. C. Chan, and S. G. Kong, "Enhanced sparsity prior model for low-rank tensor completion," *IEEE Trans. Neural Netw. Learn. Syst.*, vol. 31, no. 11, pp. 4567–4581, Nov. 2020.

[2] J. Yu, G. Zhou, C. Li, Q. Zhao, and S. Xie, "Low tensor-ring rank completion by parallel matrix factorization," *IEEE Trans. Neural Netw. Learn. Syst.*, vol. 32, no. 7, pp. 3020–3033, Jul. 2021.

[3] C.-H. Lin, R. Wu, W.-K. Ma, C.-Y. Chi, and Y. Wang, "Maximum volume inscribed ellipsoid: A new simplex-structured matrix factorization framework via facet enumeration and convex optimization," *SIAM J. Imag. Sci.*, vol. 11, no. 2, pp. 1651–1679, Jun. 2018.

[4] J. Xue, Y. Zhao, S. Huang, W. Liao, J. C.-W. Chan, and S. G. Kong, "Multilayer sparsity-based tensor decomposition for low-rank tensor completion," *IEEE Trans. Neural Netw. Learn. Syst.*, vol. 133, no. 11, pp. 1–15, Jun. 2021.

[5] M. D. Plumbley, "Algorithms for nonnegative independent component analysis," *IEEE Trans. Neural Netw.*, vol. 14, no. 3, pp. 534–543, May 2003.

[6] N. Keshava and J. F. Mustard, "Spectral unmixing," *IEEE signal Process. Mag.*, vol. 19, no. 1, pp. 44–57, Jan. 2002.

[7] W.-K. Ma, J. M. Bioucas-Dias, J. Chanussot, and P. Gader, "Signal and image processing in hyperspectral remote sensing," *IEEE Signal Process. Mag.*, vol. 31, no. 1, pp. 22–23, Jan. 2014.

[8] P. Addesso et al., "Hyperspectral image inpainting based on collaborative total variation," in *Proc. ICIP*, Beijing, China, Sep. 2017, pp. 4282–4286.

[9] W. He, H. Zhang, H. Shen, and L. Zhang, "Hyperspectral image denoising using local low-rank matrix recovery and global spatial–spectral total variation," *IEEE J. Sel. Topics Appl. Earth Observ. Remote Sens.*, vol. 11, no. 3, pp. 713–729, Mar. 2018.

[10] H. Zhang, W. He, L. Zhang, H. Shen, and Q. Yuan, "Hyperspectral image restoration using low-rank matrix recovery," *IEEE Trans. Geosci. Remote Sens.*, vol. 52, no. 8, pp. 4729–4743, Aug. 2014.

[11] C.-C. Hsu, C.-H. Lin, C.-H. Kao, and Y.-C. Lin, "DCSN: Deep compressed sensing network for efficient hyperspectral data transmission of miniaturized satellite," *IEEE Trans. Geosci. Remote Sens.*, vol. 59, no. 9, pp. 7773–7789, Sep. 2021.

[12] X. Lu, Y. Wang, and Y. Yuan, "Graph-regularized low-rank representation for destriping of hyperspectral images," *IEEE Trans. Geosci. Remote Sens.*, vol. 51, no. 7, pp. 4009–4018, Jul. 2013.

[13] W. He, H. Zhang, L. Zhang, and H. Shen, "Total-variation-regularized low-rank matrix factorization for hyperspectral image restoration," *IEEE Trans. Geosci. Remote Sens.*, vol. 54, no. 1, pp. 178–188, Jan. 2016.

[14] Y. Chang, L. Yan, T. Wu, and S. Zhong, "Remote sensing image stripe noise removal: From image decomposition perspective," *IEEE Trans. Geosci. Remote Sens.*, vol. 54, no. 12, pp. 7018–7031, Dec. 2016.

[15] C.-H. Lin, C.-Y. Chi, Y.-H. Wang, and T.-H. Chan, "A fast hyperplane-based minimum-volume enclosing simplex algorithm for blind hyperspectral unmixing," *IEEE Trans. Signal Process.*, vol. 64, no. 8, pp. 1946–1961, Apr. 2016.

[16] C. Pan, K. Tan, Q. Du, Q. Yan, and J. Ding, "Hyperspectral image destriping using unmixing-based Kriging interpolation," in *Proc. 8th Workshop Hyperspectral Image Signal Process., Evol. Remote Sens. (WHISPERS)*, Los Angeles, CA, USA, Aug. 2016, pp. 1–5.

[17] D. Cerra, R. Müller, and P. Reinartz, "Unmixing-based denoising for destriping and inpainting of hyperspectral images," in *Proc. IEEE Int. Geosci. Remote Sens. Symp. (IGARSS)*, Quebec City, QC, Canada, Jul. 2014, pp. 4620–4623.

[18] S. Wold, K. Esbensen, and P. Geladi, "Principal component analysis," *Chemometrics Intell. Lab. Syst.*, vol. 2, nos. 1–3, pp. 37–52, 1987.

[19] C.-H. Lin, Y.-C. Lin, and P.-W. Tang, "ADMM-ADAM: A new inverse imaging framework blending the advantages of convex optimization and deep learning," *IEEE Trans. Geosci. Remote Sens.*, vol. 60, pp. 1–16, 2021.

[20] Z. Zhang and S. Aeron, "Exact tensor completion using t-SVD," *IEEE Trans. Signal Process.*, vol. 65, no. 6, pp. 1511–1526, Mar. 2017.

[21] Q. Xie, Q. Zhao, D. Meng, and Z. Xu, "Kronecker-basis-representation based tensor sparsity and its applications to tensor recovery," *IEEE Trans. Pattern Anal. Mach. Intell.*, vol. 40, no. 8, pp. 1888–1902, Aug. 2018.

[22] Y. Chang, L. Yan, X. Zhao, H. Fang, Z. Zhang, and S. Zhong, "Weighted low-rank tensor recovery for hyperspectral image restoration," *IEEE Trans. Cybern.*, vol. 50, no. 11, pp. 4558–4572, Nov. 2020.

[23] T.-H. Ma, Z. Xu, D. Meng, and X.-L. Zhao, "Hyperspectral image restoration combining intrinsic image characterization with robust noise modeling," *IEEE J. Sel. Topics Appl. Earth Observ. Remote Sens.*, vol. 14, pp. 1628–1644, 2021.

[24] K. Zhang, W. Zuo, and L. Zhang, "FFDNet: Toward a fast and flexible solution for CNN-based image denoising," *IEEE Trans. Image Process.*, vol. 27, no. 9, pp. 4608–4622, Sep. 2018.

[25] L. Zhuang and J. M. Bioucas-Dias, "Fast hyperspectral image denoising and inpainting based on low-rank and sparse representations," *IEEE J. Sel. Topics Appl. Earth Observ. Remote Sens.*, vol. 11, no. 3, pp. 730–742, Mar. 2018.

[26] C.-H. Lin and J. M. Bioucas-Dias, "An explicit and scene-adapted definition of convex self-similarity prior with application to unsupervised Sentinel-2 super-resolution," *IEEE Trans. Geosci. Remote Sens.*, vol. 58, no. 5, pp. 3352–3365, May 2020.

[27] K. Dabov, A. Foi, V. Katkovnik, and K. Egiazarian, "Image denoising by sparse 3-D transform-domain collaborative filtering," *IEEE Trans. Image Process.*, vol. 16, no. 8, pp. 2080–2095, Aug. 2007.

[28] X. Zhang, "A nonconvex relaxation approach to low-rank tensor completion," *IEEE Trans. Neural Netw. Learn. Syst.*, vol. 30, no. 6, pp. 1659–1671, Jun. 2019.

[29] H. Zhang, C. Gong, J. Qian, B. Zhang, C. Xu, and J. Yang, "Efficient recovery of low-rank matrix via double nonconvex nonsmooth rank minimization," *IEEE Trans. Neural Netw. Learn. Syst.*, vol. 30, no. 10, pp. 2916–2925, Oct. 2019.

[30] M. D. Craig, "Minimum-volume transforms for remotely sensed data," *IEEE Trans. Geosci. Remote Sens.*, vol. 32, no. 3, pp. 542–552, May 1994.

[31] C.-Y. Chi, W.-C. Li, and C.-H. Lin, *Convex Optimization for Signal Processing and Communications: From Fundamentals to Applications*. Boca Raton, FL, USA: CRC Press, 2017.

[32] C.-H. Lin, W.-K. Ma, W.-C. Li, C.-Y. Chi, and A. Ambikapathi, "Identifiability of the simplex volume minimization criterion for blind hyperspectral unmixing: The no-pure-pixel case," *IEEE Trans. Geosci. Remote Sens.*, vol. 53, no. 10, pp. 5530–5546, Oct. 2015.

[33] C.-H. Lin, A. Ambikapathi, W.-C. Li, and C.-Y. Chi, "On the endmember identifiability of Craig's criterion for hyperspectral unmixing: A statistical analysis for three-source case," in *Proc. IEEE Int. Conf. Acoust., Speech Signal Process. (ICASSP)*, Vancouver, BC, Canada, May 2013, pp. 2139–2143.

[34] C.-H. Lin and J. M. Bioucas-Dias, "Nonnegative blind source separation for ill-conditioned mixtures via John ellipsoid," *IEEE Trans. Neural Netw. Learn. Syst.*, vol. 32, no. 5, pp. 2209–2223, May 2021.

[35] C.-I. Chang and Q. Du, "Estimation of number of spectrally distinct signal sources in hyperspectral imagery," *IEEE Trans. Geosci. Remote Sens.*, vol. 42, no. 3, pp. 608–619, Mar. 2004.

[36] C.-H. Lin, C.-Y. Chi, L. Chen, D. J. Miller, and Y. Wang, "Detection of sources in non-negative blind source separation by minimum description length criterion," *IEEE Trans. Neural Netw. Learn. Syst.*, vol. 29, no. 9, pp. 4022–4037, Sep. 2018.

[37] X. Zhang and M. K. Ng, "Low rank tensor completion with Poisson observations," *IEEE Trans. Pattern Anal. Mach. Intell.*, vol. 44, no. 8, pp. 4239–4251, Aug. 2021.

[38] Y. Liu, F. Shang, L. Jiao, J. Cheng, and H. Cheng, "Trace norm regularized CANDECOMP/PARAFAC decomposition with missing data," *IEEE Trans. Cybern.*, vol. 45, no. 11, pp. 2437–2448, Nov. 2015.

[39] J. Liu, P. Musialski, P. Wonka, and J. Ye, "Tensor completion for estimating missing values in visual data," *IEEE Trans. Pattern Anal. Mach. Intell.*, vol. 35, no. 1, pp. 208–220, Jan. 2013.

[40] S. Gandy, B. Recht, and I. Yamada, "Tensor completion and low-n-rank tensor recovery via convex optimization," *Inverse Problems*, vol. 27, no. 2, 2011, Art. no. 025010.

[41] Q. Shi, Y.-M. Cheung, and J. Lou, "Robust tensor SVD and recovery with rank estimation," *IEEE Trans. Cybern.*, vol. 52, no. 10, pp. 1–16, Apr. 2021.

[42] Z. Zhang, G. Ely, S. Aeron, N. Hao, and M. Kilmer, "Novel methods for multilinear data completion and de-noising based on tensor-SVD," in *Proc. IEEE CVPR*, Jun. 2014, pp. 3842–3849.

[43] C. Lu, X. Peng, and Y. Wei, "Low-rank tensor completion with a new tensor nuclear norm induced by invertible linear transforms," in *Proc. IEEE/CVF Conf. Comput. Vis. Pattern Recognit.*, Jun. 2019, pp. 5996–6004.

[44] J. A. Bengua, H. N. Phien, H. D. Tuan, and M. N. Do, "Efficient tensor completion for color image and video recovery: Low-rank tensor train," *IEEE Trans. Image Process.*, vol. 26, no. 5, pp. 2466–2479, May 2017.

[45] M. Ding, T.-Z. Huang, T.-Y. Ji, X.-L. Zhao, and J.-H. Yang, "Low-rank tensor completion using matrix factorization based on tensor train rank and total variation," *J. Sci. Comput.*, vol. 81, no. 2, pp. 941–964, Aug. 2019.

[46] L. Yuan, C. Li, D. Mandic, J. Cao, and Q. Zhao, "Tensor ring decomposition with rank minimization on latent space: An efficient approach for tensor completion," in *Proc. AAAI Conf. Artif. Intell.*, vol. 33, no. 1, Jul. 2019, pp. 9151–9158.

[47] W. He et al., "Non-local meets global: An iterative paradigm for hyperspectral image restoration," *IEEE Trans. Pattern Anal. Mach. Intell.*, vol. 44, no. 4, pp. 2089–2107, Apr. 2022.

[48] Y. Yang, Y. Feng, J. Zhang, and S. Chen, "Hyperspectral image restoration via subspace-based nonlocal low-rank tensor approximation," *IEEE Geosci. Remote Sens. Lett.*, vol. 19, pp. 1–5, 2022.

[49] J. M. P. Nascimento and J. M. Bioucas-Dias, "Vertex component analysis: A fast algorithm to unmix hyperspectral data," *IEEE Trans. Geosci. Remote Sens.*, vol. 43, no. 4, pp. 898–910, Apr. 2005.

[50] C.-H. Lin, F. Ma, C.-Y. Chi, and C.-H. Hsieh, "A convex optimization-based coupled nonnegative matrix factorization algorithm for hyperspectral and multispectral data fusion," *IEEE Trans. Geosci. Remote Sens.*, vol. 56, no. 3, pp. 1652–1667, Mar. 2018.

[51] A. Packer, "$\mathbb{NP}$-hardness of largest contained and smallest containing simplices for V- and H-polytopes," *Discrete Comput. Geometry*, vol. 28, no. 3, pp. 349–377, Aug. 2002.

[52] C.-H. Lin and T.-H. Lin, "All-addition hyperspectral compressed sensing for metasurface-driven miniaturized satellite," *IEEE Trans. Geosci. Remote Sens.*, vol. 60, pp. 1–15, 2021.

[53] S. Arora et al., "A practical algorithm for topic modeling with provable guarantees," in *Proc. Int. Conf. Mach. Learn.*, Atlanta, GA, USA, Jun. 2013, pp. 280–288.

[54] R. N. Clark et al. (2007). *USGS Digital Spectral Library Splib06a: Data Series 231*. U.S. Geological Survey. Reston, VA, USA. [Online]. Available: http://speclab.cr.usgs.gov/spectral.lib06

[55] J. Bioucas-Dias and M. A. T. Figueiredo, "Alternating direction algorithms for constrained sparse regression: Application to hyperspectral unmixing," in *Proc. 2nd Workshop Hyperspectral Image Signal Process., Evol. Remote Sens. (WHISPERS)*, Reykjavik, Iceland, Jun. 2010, pp. 1–4.

[56] J. D'Errico. (Aug. 2008). *Inpainting Nan Elements in 3-D*. MATLAB Central File Exchange, MathWorks. Natick, MA, USA. [Online]. Available: https://www.mathworks.com/matlabcentral/fileexchange/21214-inpainting-nan-elements-in-3-d

[57] J. Fan, "Multi-mode deep matrix and tensor factorization," in *Proc. Int. Conf. Learn. Represent.*, Apr. 2022, pp. 1–25.

[58] S. R. Sahoo, P. K. Panda, and P. K. Champati Ray, "Hyperspectral image analysis for iron ore discrimination in Keonjhar district, Odisha," *Int. J. Remote Sens. Geosci.*, vol. 4, no. 2, pp. 28–34, Mar. 2015.

[59] M. Simoes, J. Bioucas-Dias, L. B. Almeida, and J. Chanussot, "A convex formulation for hyperspectral image superresolution via subspace-based regularization," *IEEE Trans. Geosci. Remote Sens.*, vol. 53, no. 6, pp. 3373–3388, Jun. 2014.

[60] A. Horé and D. Ziou, "Image quality metrics: PSNR vs. SSIM," in *Proc. Int. Conf. Pattern Recognit.*, Istanbul, Turkey, Aug. 2010, pp. 2366–2369.

[61] Z. Wang and A. C. Bovik, "A universal image quality index," *IEEE Signal Process. Lett.*, vol. 9, no. 3, pp. 81–84, Aug. 2002.

[62] R. Zurita-Milla, J. G. P. W. Clevers, and M. E. Schaepman, "Unmixing-based Landsat TM and MERIS FR data fusion," *IEEE Geosci. Remote Sens. Lett.*, vol. 5, no. 3, pp. 453–457, Jul. 2008.

[63] R. H. Yuhas, A. F. Goetz, and J. W. Boardman, "Discrimination among semi-arid landscape endmembers using the spectral angle mapper (SAM) algorithm," in *Proc. Summaries 4th JPL Airborne Earth Sci. Workshop*, Pasadena, CA, USA, Dec. 1992, pp. 147–149.

[64] Z. Wang, A. C. Bovik, H. R. Sheikh, and E. P. Simoncelli, "Image quality assessment: From error visibility to structural similarity," *IEEE Trans. Image Process.*, vol. 13, no. 4, pp. 600–612, Apr. 2004.

[65] *HYDICE Free Washington DC Mall Hyperspectral Data Cube*. Accessed: Dec. 24, 2019. [Online]. Available: https://rslab.ut.ac.ir/data

[66] Y. Chang, L. Yan, and W. Liao, "HSI-DeNet: Hyperspectral image restoration via convolutional neural network," *IEEE Trans. Geosci. Remote Sens.*, vol. 57, no. 2, pp. 667–682, Feb. 2019.

[67] R. Nishii and S. Tanaka, "Accuracy and inaccuracy assessments in land-cover classification," *IEEE Trans. Geosci. Remote Sens.*, vol. 37, no. 1, pp. 491–498, Jan. 1999.

[68] C. Liu, P. Frazier, and L. Kumar, "Comparative assessment of the measures of thematic classification accuracy," *Remote Sens. Environ.*, vol. 107, no. 4, pp. 606–616, Apr. 2007.

[69] R. L. Brennan and D. J. Prediger, "Coefficient kappa: Some uses, misuses, and alternatives," *Educ. Psychol. Meas.*, vol. 41, no. 3, pp. 687–699, 1981.

[70] *ROSIS Free Pavia University Hyperspectral Data Cube*. Accessed: Nov. 15, 2020. [Online]. Available: http://www.ehu.eus/ccwintco/index.php?title=Hyperspectral_Remote_Sensing_Scenes

[71] Y. Chen, H. Jiang, C. Li, X. Jia, and P. Ghamisi, "Deep feature extraction and classification of hyperspectral images based on convolutional neural networks," *IEEE Trans. Geosci. Remote Sens.*, vol. 54, no. 10, pp. 6232–6251, Oct. 2016.

[72] Y. Fu, T. Zhang, Y. Zheng, D. Zhang, and H. Huang, "Joint camera spectral response selection and hyperspectral image recovery," *IEEE Trans. Pattern Anal. Mach. Intell.*, vol. 44, no. 1, pp. 256–272, Jan. 2020.

Chia-Hsiang Lin (Member, IEEE) received the B.S. degree in electrical engineering and the Ph.D. degree in communications engineering from the National Tsing Hua University (NTHU), Hsinchu, Taiwan, in 2010 and 2016, respectively.

From 2015 to 2016, he was a Visiting Student with Virginia Tech, Blacksburg, VA, USA. He is currently an Associate Professor with the Department of Electrical Engineering, Miin Wu School of Computing, National Cheng Kung University (NCKU), Tainan, Taiwan. He held research positions with The Chinese University of Hong Kong and the University of Lisbon (ULisboa), Lisbon, Portugal. His research interests include network science, game theory, convex geometry and optimization, quantum computing, and imaging science.

Dr. Lin was a recipient of the Best Doctoral Dissertation Award from the IEEE GRS-S in 2016. He received the Future Technology Award from National Science and Technology Council (NSTC) in 2022, the Outstanding Youth Electrical Engineer Award from The Chinese Institute of Electrical Engineering (CIEE) in 2022, the Best Young Professional Member Award from IEEE Tainan Section in 2021, and the Prize Paper Award from IEEE Geoscience and Remote Sensing Society (GRS-S) in 2020. He received the NSTC Young Scholar Fellowship, together with the EINSTEIN Grant Award from 2018 to 2023.

Yangrui Liu (Student Member, IEEE) received the B.S. degree from the Department of Communications Engineering, Feng Chia University, Taichung, Taiwan, in 2019. He is currently pursuing the Ph.D. degree with the Intelligent Hyperspectral Computing Laboratory, Institute of Computer and Communication Engineering, National Cheng Kung University, Tainan, Taiwan.

His research interests include convex optimization, deep learning, and hyperspectral imaging.

Chong-Yung Chi (Life Fellow, IEEE) received the Ph.D. degree in electrical engineering from the University of Southern California, Los Angeles, CA, USA, in 1983.

Currently, he is a Professor with the National Tsing Hua University, Hsinchu, Taiwan. He has published more than 240 technical papers, including more than 85 journal articles (mostly in IEEE TRANSACTIONS ON SIGNAL PROCESSING), three book chapters, and two books, including a recent textbook, *Convex Optimization for Signal Processing and Communications from Fundamentals to Applications* (CRC Press, 2017). His current research interests include signal processing for wireless communications, convex analysis and optimization for blind source separation, biomedical and hyperspectral image analysis, and graph signal processing.

Dr. Chi has been a Technical Program Committee Member for many IEEE sponsored and co-sponsored workshops, symposiums and conferences on signal processing and wireless communications. He received 2018 the IEEE Signal Processing Society Best Paper Award. He was an Associate Editor (AE) for four IEEE Journals, including IEEE TRANSACTIONS ON SIGNAL PROCESSING for nine years (2001–2006 and 2012–2015).

Chih-Chung Hsu (Senior Member, IEEE) received the Ph.D. degree in electrical engineering from National Tsing-Hua University (NTHU), Hsinchu, Taiwan, in 2014.

He was a Post-Doctoral Researcher with the Institute of Communications Engineering, NTHU, from 2014 to 2017. His research interests mainly lie in computer vision and machine/deep learning with applications to image and video processing.

Dr. Hsu received the first-place award of ACM Multimedia Social Media Prediction Challenge in 2017 and 2019, and the top 10% Paper Award from the IEEE International Workshop on Multimedia Signal Processing (MMSP) in 2013. He received the Best Student Paper Award from the IEEE International Conference on Image Processing (ICIP) in 2019. He also won the third place award of Learning to Drive Challenge from the IEEE International Conference on Computer Vision (ICCV) and has been invited to give a talk in it. He received the third place award of Visual Inductive Priors for Data-Efficient Computer Vision Challenge from the European Conference on Computer Vision (ECCV).

Hsuan Ren (Senior Member, IEEE) received the B.S. degree in electrical engineering from the National Taiwan University, Taipei, Taiwan, in 1994, and the M.S. and Ph.D. degrees from the University of Maryland Baltimore County, Baltimore, MD, USA, in 1998 and 2000, respectively, all in electrical engineering.

He became an Assistant Professor with National Central University, Taoyuan City, Taiwan, in 2003, where he has been an Associate Professor, since 2008. His research interests include remote sensing, target detection, signal and image processing, and pattern recognition.

Dr. Ren is a member of SPIE and the Honor Society of Phi Kappa Phi. He received National Research Council (NRC) Associateship Award and supported by the U.S. Army Edgewood Chemical Biological Center from 2000 to 2003.

Tony Q. S. Quek (Fellow, IEEE) received the B.E. and M.E. degrees in electrical and electronics engineering from the Tokyo Institute of Technology, Tokyo, Japan, in 1998 and 2000, respectively, and the Ph.D. degree in electrical engineering and computer science from the Massachusetts Institute of Technology, Cambridge, MA, USA, in 2008.

Currently, he is the Cheng Tsang Man Chair Professor with the Singapore University of Technology and Design (SUTD), Singapore, and an ST Engineering Distinguished Professor. He serves as the Director of the Future Communications Research and Development Program, the Head of ISTD Pillar, and the Deputy Director of the SUTD-ZJU IDEA. His current research topics include wireless communications and networking, network intelligence, nonterrestrial networks, and 6G.

Dr. Quek is a fellow of the Academy of Engineering Singapore. He was honored with the 2008 Philip Yeo Prize for Outstanding Achievement, the 2012 IEEE William R. Bennett Prize, the 2015 SUTD Outstanding Education Awards, the 2016 IEEE Signal Processing Society Young Author Best Paper Award, the 2017 CTTC Early Achievement Award, the 2017 IEEE ComSoc AP Outstanding Paper Award, the 2020 IEEE Communications Society Young Author Best Paper Award, the 2020 IEEE Stephen O. Rice Prize, the 2020 Nokia Visiting Professor, and the 2022 IEEE Signal Processing Society Best Paper Award.